*J. Fluid Mech.* (2008), *vol.* 606, *pp.* 239–273.  
doi:10.1017/S0022112008001912 Printed in the United Kingdom

# Instability and breakdown of a vertical vortex pair in a strongly stratified fluid

MICHAEL L. WAITE† AND PIOTR K. SMOLARKIEWICZ

National Center for Atmospheric Research, PO Box 3000, Boulder, CO 80307-3000, USA

(Received 26 March 2007 and in revised form 29 March 2008)

The dynamics of a counter-rotating pair of columnar vortices aligned parallel to a stable density gradient are investigated. By means of numerical simulation, we extend the linear analyses and laboratory experiments of Billant & Chomaz (*J. Fluid Mech.* vol. 418, p. 167; vol. 419, pp. 29, 65 (2000)) to the fully nonlinear, large-Reynolds-number regime. A range of stratifications and vertical length scales is considered, with $Fr_h < 0.2$ and $0.1 < Fr_z < 10$. Here $Fr_h \equiv U/(NR)$ and $Fr_z \equiv Uk_z/N$ are the horizontal and vertical Froude numbers, $U$ and $R$ are the horizontal velocity and length scales of the vortices, $N$ is the Brunt–Väisälä frequency, and $2\pi/k_z$ is the vertical wavelength of a small initial perturbation. At early times with $Fr_z < 1$, linear predictions for the zigzag instability are reproduced. Short-wavelength perturbations with $Fr_z > 1$ are found to be unstable as well, with growth rates only slightly less than those of the zigzag instability but with very different structure. At later times, the large-Reynolds-number evolution diverges profoundly from the moderate-Reynolds-number laboratory experiments as the instabilities transition to turbulence. For the zigzag instability, this transition occurs when density perturbations generated by the vortex bending become gravitationally unstable. The resulting turbulence rapidly destroys the vortex pair. We derive the criterion $\eta/R \approx 0.2/Fr_z$ for the onset of gravitational instability, where $\eta$ is the maximum horizontal displacement of the bent vortices, and refine it to account for a finite twisting disturbance. Our simulations agree for the fastest growing wavelengths $0.3 < Fr_z < 0.8$. Short perturbations with $Fr_z > 1$ saturate at low amplitude, preserving the columnar structure of the vortices well after the generation of turbulence. Viscosity is shown to suppress the transition to turbulence for Reynolds number $Re \lesssim 80/Fr_h$, yielding laminar dynamics and, under certain conditions, pancake vortices like those observed in the laboratory.

## 1. Introduction

Vortices are ubiquitous in the atmosphere and oceans. The question of their stability has important practical and theoretical consequences, since instability provides a mechanism for energy transfer from large to small scales where dissipation occurs. A counter-rotating columnar vortex pair oriented parallel to a stable background density gradient is an elementary model for complicated geophysical vortical flows. Recent laboratory experiments and linear analyses have shown that such vortices are unstable to three-dimensional perturbations when density stratification is strong (Billant & Chomaz 2000*a*, *b*, *c*; see also Otheguy, Billant & Chomaz 2006*a*, *b* for the case of a co-rotating vortex pair). Here we examine the nonlinear, large-Reynolds-number

† Present address: University of Victoria, PO Box 3060 Stn CSC, Victoria, BC V8W 3R4, Canada

evolution of these perturbations, from linear instability at early times to dissipation (possibly turbulent) at late times. We neglect Coriolis effects as a first approximation to the atmospheric mesoscale and oceanic submesoscale, which are characterized by strong stratification but only moderate rotation.

Early work on vortex instability was concerned with neutrally stratified fluids. Lord Kelvin (1880) studied disturbances to columnar Rankine vortices (Kelvin waves), and found them to be neutrally stable. Interest in the instability of such disturbances was revived by Crow (1970), who found that a pair of counter-rotating vortices is unstable to axially varying displacements of the vortex cores (bending waves). Unstable bending waves grow via resonance with the oscillating strain field induced by each vortex on the other. The corresponding growth rate is maximum at axial scales much larger than the vortex radii. Instabilities also exist at smaller axial scales, driven by resonances with Kelvin waves of more complicated radial structure than the bending waves. These instabilities have been studied extensively in the context of a vortex filament in an externally imposed strain field (Moore & Saffman 1975; Tsai & Widnall 1976; Robinson & Saffman 1984; Vladimirov & Il'in 1988). A separate approach has focused on the instability of two-dimensional flows with elliptical streamlines to three-dimensional perturbations (Bayly 1986; Pierrehumbert 1986; Waleffe 1990). Both sets of short-wave instabilities are referred to as elliptic instabilities (e.g. Kerswell 2002). Laboratory experiments by Thomas & Auerbach (1994) and Leweke & Williamson (1998) demonstrated that a counter-rotating vortex pair undergoes an antisymmetric short-wave instability. The latter authors suggested that the instability is driven by the resonance mechanism of the elliptic instability, and called it a cooperative elliptic instability. Linear simulations and analysis (Billant, Brancher & Chomaz 1999; Le Dizès & Laporte 2002; Sipp & Jacquin 2003) and direct numerical simulations (Laporte & Corjon 2000) support this view.

Density stratification modifies the elliptic instability by changing the dispersion relation of the Kelvin waves. Miyazaki & Fukumoto (1992) showed that the elliptic instability of a strained uniform vortex aligned with a stable density gradient is inhibited by stratification and disappears when the Brunt–Väisälä frequency $N$ exceeds the vorticity. However, they found that other instabilities connected with higher-order resonances emerge and persist at strong stratifications. For the case of a vortex pair, Billant & Chomaz (2000*c*) showed that the cooperative elliptic instability is suppressed when $Fr_h < 0.2$. Here $Fr_h \equiv U/(RN)$, where $U$ and $R$ are the propagation speed and radius of the vortex pair (defined in § 2.1 below). At these strong stratifications they found a distinct antisymmetric instability, which they call the zigzag instability. Like that of Crow (1970), the zigzag instability bends and twists the vortex cores horizontally with little change to their internal structure. It has been studied with laboratory experiments, multiple-scale analysis, and linear numerical simulations (Billant & Chomaz 2000*a*, *b*, *c*, respectively).

The linear analysis of Billant & Chomaz (2000*b*) employs an asymptotic expansion in small $Fr_h$ and $Fr_z \equiv Uk_z/N$, where $k_z$ is the vertical wavenumber of the perturbation to the vortex pair. It is therefore restricted to $k_z \ll N/U$, or vertical scales much larger than $2\pi U/N$. In this strongly stratified regime, the dimensionless equations for vortex motion describe decoupled layers of two-dimensional solenoidal flow at lowest order in $Fr_h$ and $Fr_z$ (Drazin 1961; Riley, Metcalfe & Weissman 1981; Lilly 1983). Buoyancy and vertical velocity are slaved to the horizontal velocity via hydrostatic balance, and gravity waves are filtered out. Billant & Chomaz (2000*b*) showed that the slaved vertical velocity induced by a bending and twisting perturbation of the dipole stretches the vorticity in a way that amplifies the perturbation. This is the basic

mechanism of the zigzag instability. Numerical simulations of the linear problem are in broad agreement with the analytical work (Billant & Chomaz 2000*c*). Given that the fastest growing vertical wavenumber has $Fr_z \approx 0.7$, and thus is not formally small, this agreement is remarkable.

In the laboratory, the zigzag instability grows to large amplitude while remaining laminar (Billant & Chomaz 2000*a*). Vortices at different vertical levels, with thicknesses corresponding to $Fr_z \approx 0.7$, appear to decouple from one another and evolve independently. Consequently, it has been proposed (e.g. Billant & Chomaz 2000*a*) that the zigzag instability may explain the emergence of layering in simulations of homogeneous stratified turbulence, which has been observed for columnar vortex forcing (e.g. Herring & Métais 1989; Waite & Bartello 2004; Lindborg 2006), decaying Taylor–Green vortices (Riley & deBruynKops 2003), and stratified shear layers (Basak & Sarkar 2006). However, such simulations are often far from laminar, exhibiting three-dimensional turbulent motion at scales of $O(U/N)$ when the Reynolds number is sufficiently large (for a discussion of the strongly stratified limiting dynamics with $Fr_z = O(1)$, see Billant & Chomaz 2001). Does the zigzag instability likewise transition to turbulence at large Reynolds number? The experiments of Billant & Chomaz (2000*a*), where $Re \equiv UR/\nu \approx 400$ ($\nu$ is the kinematic viscosity), do not preclude this possibility.

In this work, we use numerical simulations to examine the full nonlinear evolution of perturbations to a counter-rotating vortex pair in a strongly stratified fluid. Our primary aim is to evaluate how the linear predictions of Billant & Chomaz (2000*b*, *c*) are manifested at finite amplitude, and particularly to determine whether the zigzag instability saturates and breaks down into turbulence (and if so, how). We also consider the dynamics of short-wave perturbations with $Fr_z > 1$, which have stability properties that are distinct from the zigzag instability. We obtain finite-amplitude dynamics that are significantly different from the laboratory findings of Billant & Chomaz (2000*a*); indeed, the vortices break down into turbulence for every $Fr_z$ considered. We argue, however, that these results are consistent with the high Reynolds number of our simulations.

In order to explore a wide region of parameter space, we have conducted a large set of numerical experiments ($\approx 50$), each employing $O(10^6)$–$O(10^7)$ grid points and $O(10^3)$ time steps. The temporal and spatial resolution adopted is adequate to capture the large-scale aspects of the instability and breakdown of the vortex pair, while leaving the handling of grid-scale features to a subgrid-scale model. Direct numerical simulation (DNS) with Reynolds number high enough to capture not only secondary instabilities but also the resulting transition to turbulence would require two orders of magnitude more computing resources. Given the large number of simulations performed here, an exclusively DNS approach was not practical. To minimize the computational effort and maximize the effective Reynolds number of our simulations, we employ the implicit large-eddy-simulation (ILES) approach (Margolin, Rider & Grinstein 2006*a*; Grinstein, Margolin & Rider 2007) that exploits the properties of high-resolution non-oscillatory finite-volume methods to mimic spectral viscosities of standard LES (Domaradzki, Xiao & Smolarkiewicz 2003). The suppression of secondary instabilities by viscosity is examined with DNS and LES, which verify the accuracy of our approach.

In the following section we outline our equations, methodology, and numerical model. In § 3, we present simulations of the vortex pair perturbed at distinct vertical wavelengths spanning a wide range of $Fr_z$ on both sides of unity. At early times and for $Fr_z < 1$, the growth rates and instability structures agree well with the linear

analysis of Billant & Chomaz (2000*c*). Smaller perturbations, however, behave very differently. In all cases, the linear instability ultimately saturates and gives way to turbulence. Viscosity is shown to suppress the development of turbulence in line with the laboratory experiments. Discussion and conclusions are given in § 4. Sensitivity tests to model set-up, resolution, and numerics are described in Appendix A, and mathematical details of the analysis in § 3 are given in Appendix B.

## 2. Formulation of the problem

### 2.1. *Equations and initial conditions*

Following Billant & Chomaz (2000*b*, *c*), we consider a uniformly stratified Boussinesq fluid with a Lamb–Chaplygin vortex dipole (Lamb 1895; Chaplygin 1903). The Navier–Stokes equations with the Boussinesq approximation are

$$\frac{\mathrm{D}\boldsymbol{u}}{\mathrm{D}t} = -\nabla\phi - g\frac{\rho}{\rho_0}\hat{\boldsymbol{e}}_3 + \nu\nabla^2\boldsymbol{u}, \tag{2.1a}$$

$$\frac{\mathrm{D}\rho}{\mathrm{D}t} = -\frac{\mathrm{d}\overline{\rho}}{\mathrm{d}z}\,w + \kappa\nabla^2\rho, \tag{2.1b}$$

$$\nabla\cdot\boldsymbol{u} = 0, \tag{2.1c}$$

where $\mathrm{D}/\mathrm{D}t \equiv \partial/\partial t + \boldsymbol{u}\cdot\nabla$, $\nabla \equiv \hat{\boldsymbol{e}}_1\partial/\partial x + \hat{\boldsymbol{e}}_2\partial/\partial y + \hat{\boldsymbol{e}}_3\partial/\partial z$, $\boldsymbol{u} \equiv u\hat{\boldsymbol{e}}_1 + v\hat{\boldsymbol{e}}_2 + w\hat{\boldsymbol{e}}_3$ is the velocity, $\rho$ is the density perturbation from a vertically varying background profile $\overline{\rho}(z)$, $\rho_0$ is a constant reference density, $\phi$ is the dynamic pressure divided by $\rho_0$, $g$ is the gravitational acceleration, and $\nu$ is the kinematic viscosity. Density stratification is assumed to result from the variation of salt concentration in water, and so $\kappa$ is the corresponding diffusivity. The Brunt–Väisälä frequency $N$ is given by

$$N^2 \equiv -\frac{g}{\rho_0}\frac{\mathrm{d}\overline{\rho}}{\mathrm{d}z}, \tag{2.2}$$

and is assumed to be constant.

The Lamb–Chaplygin dipole is an exact solution to the two-dimensional Euler equations and therefore also, when oriented vertically, to (2.1) with $\nu \equiv \kappa \equiv 0$. It gives a good approximation to the vortices generated by the opening of a pair of flaps in laboratory experiments (cf. Leweke & Williamson 1998; Billant & Chomaz 2000*a*). In cylindrical polar coordinates $(r, \theta, z)$, where

$$x - x_0 \equiv r\cos\theta, \tag{2.3a}$$

$$y - y_0 \equiv r\sin\theta, \tag{2.3b}$$

the dipole is defined by its two-dimensional stream function $S_0$, where

$$S_0(r,\theta) \equiv \begin{cases} \dfrac{-2UR}{\mu_1 J_0(\mu_1)} J_1(\mu_1 r/R)\sin\theta, & r \leqslant R, \\ -Ur\left(1 - \dfrac{R^2}{r^2}\right)\sin\theta, & r > R, \end{cases} \tag{2.4}$$

or its vertical component of vorticity (hereafter vertical vorticity)

$$\omega_{z0}(r,\theta) \equiv -\nabla_h^2 S_0 \equiv \begin{cases} \dfrac{\mu_1^2}{R^2} S_0, & r \leqslant R, \\ 0, & r > R, \end{cases} \tag{2.5}$$

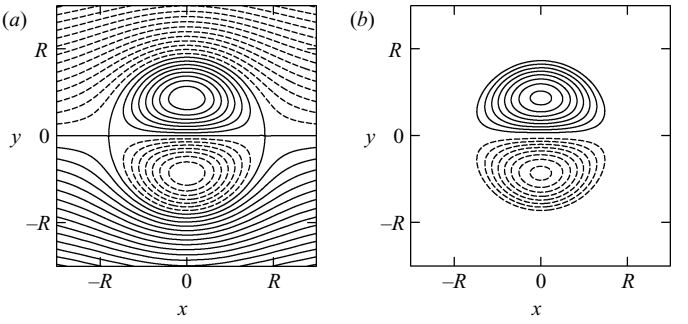


FIGURE 1. Horizontal $(x,y)$ slices of Lamb–Chaplygin stream function $S_0$ $(a)$ and vertical vorticity $\omega_{z0}$ $(b)$ in the frame moving with the dipole with $x_0 = y_0 = 0$ in (2.3). Negative contours are dashed. The direction of propagation is to the right.

where $U$ is the dipole propagation speed, $R$ is its radius, $J_0$ and $J_1$ are the zeroth- and first-order Bessel functions, $\mu_1 = 3.8317$ is the first root of $J_1$, and $\nabla_h \equiv \hat{\boldsymbol{e}}_1 \partial/\partial x + \hat{\boldsymbol{e}}_2 \partial/\partial y$. Here $S_0$ is related to the horizontal velocity by $\boldsymbol{u}_{h0} \equiv \nabla_h \times (S_0 \hat{\boldsymbol{e}}_3)$† and $\omega_z$ is the vertical component of the vorticity $\boldsymbol{\omega} \equiv \nabla \times \boldsymbol{u}$. The dipole, which has $\rho \equiv 0$ and $w \equiv 0$, consists of a pair of counter-rotating vertical vortices inside a cylinder of radius $R$ centred at $(x_0,y_0)$; outside the cylinder, the flow is irrotational. Equations (2.4) and (2.5) are valid in a frame of reference moving with the dipole; in the laboratory frame, the dipole moves with speed $U$ in the direction of positive $x$. The maximum speed occurs at $r = 0$ and is equal to $(1 - 1/J_0(\mu_1))U \approx 3.5\,U$ in the laboratory frame. The structure of the dipole in the moving frame is illustrated in figure 1.

In a stratified fluid, the vortex pair (2.4) is a dipole of potential vorticity (PV)

$$\Pi \equiv \frac{1}{\rho_0} \boldsymbol{\omega} \cdot \nabla \ (\overline{\rho} + \rho)\,, \tag{2.6}$$

which satisfies

$$\frac{\mathrm{D}\Pi}{\mathrm{D}t} = 0, \tag{2.7}$$

when $\nu \equiv \kappa \equiv 0$. The Lamb–Chaplygin dipole has PV $\Pi_0 \equiv -\omega_{z0} N^2/g$. The strength of the stratification is expressed by the smallness of the horizontal Froude number, $Fr_h = U/(NR)$, which is the ratio of the buoyancy time scale $1/N$ and the vortex turnover time $R/U$. Laboratory experiments and linear stability analysis indicate that the zigzag instability requires $Fr_h < 0.2$; at larger Froude numbers, the elliptic instability dominates (Billant & Chomaz 2000*a*, *c*). We restrict our attention to this strongly stratified regime. Diffusive effects are characterized by the Reynolds number, $Re = UR/\nu$, and Schmidt number $Sc \equiv \nu/\kappa$. Since the initial flow and Brunt–Väisälä frequency are independent of $z$, perturbations to the Lamb–Chaplygin dipole may be expressed as a sum of modes of the form

$$\begin{pmatrix} \hat{\boldsymbol{u}} \\ \hat{\rho} \\ \hat{\phi} \end{pmatrix} (x, y, t)\, \mathrm{e}^{\mathrm{i}k_z z} + \text{c.c.}, \tag{2.8}$$

† This definition of the stream function follows Batchelor (1967), and differs in sign from that of Billant & Chomaz (2000*b*).

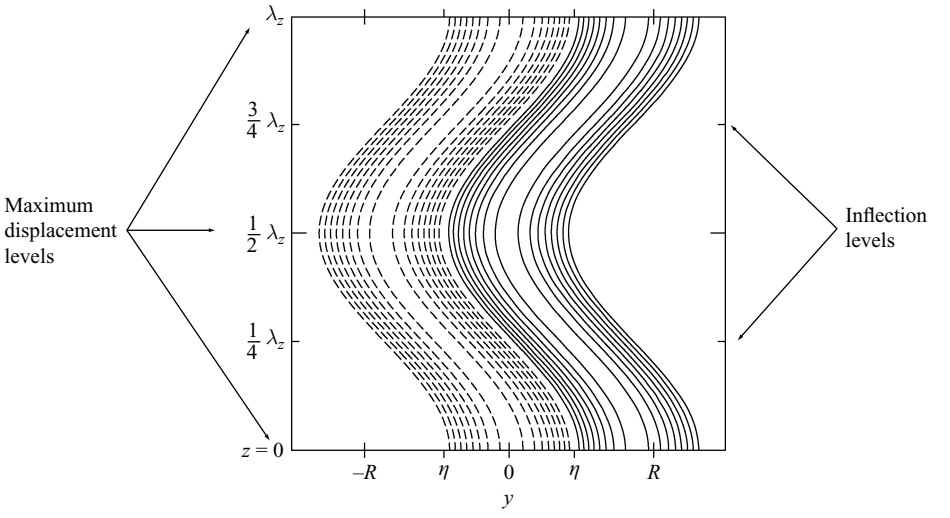


FIGURE 2. Vertical $(y,z)$ slice of the perturbed vertical vorticity $\omega_{0z}$ given by (2.5) with $x_0=0$, $y_0=\eta\cos(k_z z)$, $\eta=R/2$, shown on the plane $x=0$. Contours are as in figure 1.

where c.c. is the complex conjugate. The vertical wavenumber $k_z$ of a single mode defines a vertical Froude number, $Fr_z=Uk_z/N$; thus $Fr_z$ is the dimensionless perturbation wavenumber. In the limit of small perturbations, the dependence on $t$ in (2.8) has the form $\mathrm{e}^{\sigma t}$.

At $t=0$, we perturb the Lamb–Chaplygin dipole by displacing its centre in the $y$-direction with a cosine in the vertical, i.e. by taking

$$x_0=0, \quad y_0=\eta\cos(k_z z), \tag{2.9}$$

in (2.3). The perturbed dipole has the form

$$S_0^*(x^*, y^*-\eta^*\cos z^*)=S_0^*(x^*, y^*)-\eta^*\cos z^*\frac{\partial S_0^*}{\partial y^*}+\frac{1}{2}\eta^{*2}\cos^2 z^*\frac{\partial^2 S_0^*}{\partial y^{*2}}+O(\eta^{*3}), \tag{2.10}$$

where $*$ denotes a dimensionless variable, $S_0^*\equiv S_0/(UR)$, $\{x^*, y^*, \eta^*\}\equiv\{x, y, \eta\}/R$, and $z^*\equiv k_z z$. The perturbation therefore excites only a single vertical mode (i.e. it has the form of equation (2.8)) at first order in $\eta/R$; higher harmonics $n\,k_z$ are excited at higher orders $(\eta/R)^n$. Our initial displacement is small, with $\eta/R=0.001$. The largest displacement is at $z=0, \lambda_z/2, \ldots$, and so we refer to these levels as maximum displacement levels; likewise, the largest curvature is at $z=\lambda_z/4, 3\lambda_z/4, \ldots$, which we call the inflection levels (see figure 2). Our perturbation of a single mode mimics the forced experiment of Billant & Chomaz (2000*a*), and their leading-order perturbation analysis (Billant & Chomaz 2000*b*); in the forced laboratory experiment, a particular vertical scale was excited by applying strips of tape to the flaps.

### 2.2. *Numerical model and experimental set-up*

The governing equations (2.1) are integrated numerically using a second-order-accurate, semi-implicit, flux-form Eulerian, non-oscillatory forward-in-time (NFT) approach, whose theory, implementation and applications are broadly documented in the literature (see Smolarkiewicz & Margolin 1998; Smolarkiewicz & Prusa 2002, 2005, and references therein). We assume that all variables are co-located – a choice

important for the efficacy of the semi-implicit integrals (see Smolarkiewicz *et al.* 2007) – and write the resulting finite-difference approximations in a compact symbolic form,

$$\Psi_i^{n+1} = \mathscr{A}_i(\widetilde{\Psi}) + 0.5\Delta t F_i^{n+1} \ . \tag{2.11}$$

Here $\Psi$ represents a dependent prognostic variable (i.e. a velocity component or $\rho$); $F$ is the associated right-hand side in (2.1); $\mathscr{A}$ denotes a fully second-order-accurate two-time-level non-oscillatory advection transport algorithm; and $\widetilde{\Psi}_i \equiv \Psi_i^n + 0.5\Delta t F_i^n$. The indices $\boldsymbol{i}$ and $n$ denote the spatial and temporal location on the grid, and $\Delta t$ is a temporal increment. Transporting the auxiliary field $\widetilde{\Psi}$ rather than the fluid variable alone has been shown to be important for the accuracy and stability of forward-in-time approximations (Smolarkiewicz & Margolin 1993). The NFT algorithm (2.11) is implemented in the high-performance model EULAG (Smolarkiewicz & Margolin 2007), in which the transport operator $\mathscr{A}$ employs the monotone flux-form MPDATA algorithm (Smolarkiewicz & Grabowski 1990; Smolarkiewicz & Margolin 1998; Smolarkiewicz 2006). For inviscid dynamics, all prognostic equations in (2.1) are integrated with (2.11) using, effectively, the trapezoidal rule (Smolarkiewicz & Margolin 1993), thus treating all forcings on the right-hand side implicitly. Viscous terms are evaluated explicitly to the first order, and are included in $\mathscr{A}$ (Smolarkiewicz *et al.* 2007). The semi-implicit NFT formulation leads to a complicated elliptic problem for pressure (see Appendix A in Prusa & Smolarkiewicz 2003, for the complete description), which is solved iteratively using the preconditioned generalized conjugate-residual approach, a non-symmetric Krylov-subspace solver (Smolarkiewicz & Margolin 2000). For recent succinct reviews of the complete model numerics in diverse oceanic and atmospheric applications, the interested reader is referred to Warn-Varnas *et al.* (2007) and Smolarkiewicz *et al.* (2007).

There are a few important benefits, relevant for this study, of formulating and integrating the governing partial differential equations as described. First, transporting only perturbations of density, while retaining the convective derivative of the background state on the right-hand side, assures conservation of density perturbations with accuracy to round-off error (section 3a in Smolarkiewicz, Margolin & Wyszogrodzki 2001), tantamount to preventing dilution of the background stratification due to the implicit viscosity of non-oscillatory advection. Second, truncation terms of non-oscillatory finite-volume schemes such as MPDATA have been shown to act as an effective subgrid-scale turbulence model, allowing efficient implicit LES (Margolin, Smolarkiewicz & Wyszogrodzki 2002, Domaradzki *et al.* 2003; Margolin *et al.* 2006*a*; Grinstein *et al.* 2007; Smolarkiewicz & Margolin 2007). These schemes inhibit spurious grid-scale oscillations by construction, supplying a minimal amount of dissipation necessary to keep the solution physical. As a result, viscosity and diffusion are not required for nonlinear numerical stability, and so we let $\nu$ and $\kappa$ be non-zero only when considering the effects of finite $Re$ and $Sc$. At a given resolution, the effective viscosity of the scheme in the inviscid case has been shown to be at least an order of magnitude smaller than the minimum explicit viscosity required for DNS (Smolarkiewicz & Prusa 2002). Furthermore, the effective viscosity is adaptive; the corresponding dissipation rate decreases as one approaches the DNS regime, where it is much less than the explicit viscous dissipation rate (Margolin, Smolarkiewicz & Wyszogradzki 2006*b*). Sensitivity to resolution and comparisons with a spectral-transform model and standard LES model are given in Appendix A.2, where the ILES approach is shown to adequately capture the large-scale features of the instability and breakdown of the vortex pair. For a validation against a related

| Run | $Fr_h$ | $Fr_z$ | $\lambda_z/R$ | $\Delta z/\Delta x$ | $\lambda_z/\Delta z$ |
|---|---|---|---|---|---|
| 1 | 0.1 | 0.157 | 4 | 1 | 100 |
| 2 | 0.1 | 0.314 | 2 | 1 | 50 |
| 3 | 0.1 | 0.393 | 1.6 | 1 | 40 |
| 4 | 0.1 | 0.449 | 1.4 | 1 | 35 |
| 5 | 0.1 | 0.628 | 1 | 1 | 25 |
| 6 | 0.1 | 0.785 | 0.8 | 1 | 20 |
| 7 | 0.1 | 0.896 | 0.7 | 0.875 | 20 |
| 8 | 0.1 | 1.05 | 0.6 | 0.75 | 20 |
| 9 | 0.1 | 1.26 | 0.5 | 0.625 | 20 |
| 10 | 0.1 | 1.80 | 0.35 | 0.4375 | 20 |
| 11 | 0.1 | 2.51 | 0.25 | 0.3125 | 20 |
| 12 | 0.1 | 5.02 | 0.125 | 0.15625 | 20 |
| 13 | 0.05 | 0.157 | 2 | 1 | 50 |
| 14 | 0.05 | 0.314 | 1 | 1 | 25 |
| 15 | 0.05 | 0.628 | 0.5 | 0.625 | 20 |
| 16 | 0.05 | 0.785 | 0.4 | 0.5 | 20 |
| 17 | 0.05 | 1.05 | 0.3 | 0.375 | 20 |
| 18 | 0.05 | 1.26 | 0.25 | 0.3125 | 20 |
| 19 | 0.05 | 1.80 | 0.175 | 0.21875 | 20 |
| 20 | 0.05 | 2.51 | 0.125 | 0.15625 | 20 |

TABLE 1. Parameters used in the inviscid simulations. Runs 1–12 are the primary simulations at $Fr_h = 0.1$, and 13–20 are analogous runs at $Fr_h = 0.05$.

laboratory experiment with density stratification and gravity waves see Wedi & Smolarkiewicz (2006).

Boundary conditions for $(\boldsymbol{u}, \phi, \rho)$ are periodic in all directions with periods $(L_x, L_y, L_z)$. In the horizontal, $L_x$ and $L_y$ are set equal to $20R$, which is a factor of two larger than that used in the linear simulations of Billant & Chomaz (2000*c*); we require a larger domain to ensure that gravity waves, which are generated by the nonlinear evolution of the vortex pair, do not interact with the vortices after exiting and re-entering the domain. In the vertical, $L_z$ is set to one perturbation wavelength $\lambda_z \equiv 2\pi/k_z$. Since only a single wavelength is perturbed, the triadic wavevector interactions of the quadratic nonlinearity in (2.1) are unable to excite larger vertical scales, making, in theory, a deeper domain unnecessary. We have verified that long-time integrations with deeper model domains are consistent with this theoretical prediction. The dipole propagation speed $U$ is chosen such that the vortex turnover time $R/U$ is the unit time scale, and so $Fr_h$ is varied by changing $N$ only. We consider $Fr_h = 0.1$ and 0.05, which are both below the zigzag instability threshold of 0.2 (the laboratory value of 0.19 is also used for comparison with Billant & Chomaz 2000*a*). We concentrate below on the results for $Fr_h = 0.1$; unless otherwise stated, behaviour at a given $Fr_z$ is qualitatively similar to that at $Fr_h = 0.05$. The parameters for each simulation are given in tables 1 and 2.

A wide range of perturbation wavenumbers $k_z$ is examined: $Fr_z$ varies by powers of 2 from $O(0.1)$ to $O(10)$, and additional $Fr_z$ are included in parameter-space regions of interest. The horizontal grid spacing is $\Delta x = R/25$, while the vertical grid spacing $\Delta z$ is chosen as the minimum of $\Delta x$ and $\lambda_z/20$. The vertical wavelength is therefore resolved with at least 20 grid points, while the aspect ratio of the grid $\Delta z/\Delta x \leqslant 1$. Though it would be preferable to employ an isotropic grid in all simulations, the computational expense is prohibitive. The robustness of our results to increasing

| Run | $Fr_h$ | $Fr_z$ | $\lambda_z/R$ | $\Delta z/\Delta x$ | $\lambda_z/\Delta z$ | $Re$ | $Sc$ | $l_d/\Delta x$ |
|---|---|---|---|---|---|---|---|---|
| 21 | 0.19 | 0.628 | 1.9 | 0.989 | 48 | 365 | 685 | 1.8 |
| 22 | 0.19 | 0.628 | 1.9 | 0.989 | 48 | 450 | 685 | 1.6 |
| 23 | 0.1 | 0.628 | 1 | 1 | 25 | 365 | 685 | 1.8 |
| 24 | 0.1 | 0.628 | 1 | 1 | 25 | 600 | 685 | 1.2 |
| 25 | 0.1 | 0.628 | 1 | 1 | 25 | 700 | 685 | 1.0 |
| 26 | 0.1 | 0.628 | 1 | 1 | 25 | 1000 | 685 | 0.75 |
| 27 | 0.05 | 0.628 | 0.5 | 0.625 | 20 | 700 | 685 | 1.3 |
| 28 | 0.05 | 0.628 | 0.5 | 0.625 | 20 | 1200 | 685 | 0.65 |
| 29 | 0.05 | 0.628 | 0.5 | 0.625 | 20 | 1400 | 685 | 0.56 |
| 30 | 0.19 | 0.628 | 1.9 | 0.989 | 48 | 450 | 1 | 1.6 |
| 31 | 0.19 | 0.628 | 1.9 | 0.989 | 48 | 600 | 1 | 1.2 |
| 32 | 0.1 | 0.628 | 1 | 1 | 25 | 700 | 1 | 1.0 |
| 33 | 0.1 | 0.628 | 1 | 1 | 25 | 800 | 1 | 0.91 |
| 34 | 0.05 | 0.628 | 0.5 | 0.625 | 20 | 1600 | 1 | 0.50 |
| 35 | 0.05 | 0.628 | 0.5 | 0.625 | 20 | 1800 | 1 | 0.46 |

TABLE 2. Parameters used in the viscous simulations. Runs 21–29 have $Sc = 685$, and runs 30–35 have $Sc = 1$. The Kolmogorov scale $l_d$ is defined in § 3.3.

resolution is demonstrated in Appendix A. The time step is set to $\Delta t = 0.125\Delta x/U$, which ensures an initial Courant number $|\boldsymbol{u}|_{\max}\,\Delta t/\Delta x$ of 0.35. The integration length varies with $Fr_z$ but continues for several turnover times past the time of maximum energy dissipation. In most instances, $\nu$ and $\kappa$ are set to 0 to maximize the effective Reynolds number. For a subset of cases (runs 21–35) we consider finite Reynolds numbers, with $Sc = 1$ and 685, the latter representative of salt in water.

## 3. Results

The evolution of the vortices proceeds through three phases: adjustment to the initial conditions, exponential growth of the perturbation, and nonlinear evolution. These different regimes are manifested in the evolution of the fluctuation energy, defined as follows. The velocity can be separated into its vertical average $\overline{\boldsymbol{u}}$ and fluctuation $\boldsymbol{u}' \equiv \boldsymbol{u} - \overline{\boldsymbol{u}}$, where

$$\overline{\boldsymbol{u}} \equiv \frac{1}{L_z}\int \boldsymbol{u}\,\mathrm{d}z\,. \tag{3.1}$$

The kinetic energy

$$E_K \equiv \frac{1}{V}\int \boldsymbol{u}^2\,\mathrm{d}\boldsymbol{x}, \tag{3.2}$$

where $V \equiv L_x L_y L_z$, therefore has vertical average and fluctuation contributions given by

$$\overline{E}_K \equiv \frac{1}{V}\int \overline{\boldsymbol{u}}^2\,\mathrm{d}\boldsymbol{x}, \quad E'_K \equiv \frac{1}{V}\int \boldsymbol{u}'^2\,\mathrm{d}\boldsymbol{x}\,. \tag{3.3}$$

A similar decomposition can be applied to the available potential energy

$$E_P \equiv \frac{1}{V}\frac{g^2}{\rho_0^2 N^2}\int \rho^2\,\mathrm{d}\boldsymbol{x}\,. \tag{3.4}$$

The unperturbed Lamb–Chaplygin dipole has $E'_K \equiv 0$ and $\overline{E}_P \equiv E'_P \equiv 0$. Three-dimensional linear instability leads to exponential growth in $E'_K$ and $E'_P$ ($\overline{E}_P$ remains

$\ll E'_P$). In what follows, fluctuations from the vertical average are employed in place of deviations from the Lamb–Chaplygin dipole, a relation that is exact for all non-zero vertical wavenumbers. The evolution of two-dimensional perturbations to (2.4) requires a more careful decomposition and is not considered here. The symmetric Lamb–Chaplygin dipole is believed to be stable to two-dimensional perturbations, though subtle questions remain unanswered (see Meleshko & van Heijst 1994).

Time series of $\overline{E}_K$, $E'_K$ and $E'_P$ are plotted in figure 3 for a selection of $Fr_z$ ranging from 0.157 to 5.02 by factors of 2. At $t=0$, $E'_K/E_0 = O(10^{-6})$, so the initial fluctuation energy implied by the sinusoidal displacement of the vortices is indeed small. Since the perturbation is not in hydrostatic balance, there is an initial transfer of kinetic to potential energy. Oscillations in $E'_P$ are visible at early times for small $Fr_z$ and are due to internal gravity waves excited by the adjustment of the fluid to hydrostatic balance.

### 3.1. *Linear regime*

After the initial adjustment, the fluctuation kinetic and potential energies grow exponentially for several turnover times (with the exception of $Fr_z = 5.02$). The growth rates are plotted against $Fr_z$ in figure 4. They agree well with the linear calculations of Billant & Chomaz (2000*c*) for $Fr_z < 1$ (shorter perturbations were not considered in their work), reaching a maximum of nearly $0.7R/U$ for $0.6 < Fr_z < 0.7$. The dependence on $Fr_h$ is secondary. The growth rate decreases as $Fr_z$ is increased above 0.7, and has a local minimum at $Fr_z \approx 2$. Further increase in $Fr_z$ results in a small increase in $\sigma$, which is around 80% of the maximum zigzag growth rate at $Fr_z = 2.51$. Since the linear zigzag instability theory of Billant & Chomaz (2000*b*) requires $Fr_z < 1$, it appears that a distinct short-wave instability is acting at vertical scales with $k_z > N/U$. When $Fr_z = 5.02$ (figure 3*f*), the fluctuation energy grows rapidly but not exponentially, so we have not reported a growth rate in this case. The oscillations in the time series are robust even when small random perturbations are employed, suggesting that they are not a transient response to the initial perturbation but rather are due to the emergence of an unstable oscillatory mode (i.e. with non-zero imaginary part of $\sigma$) at these large $Fr_z$. By contrast, the small deviations from exponential growth evident in figure 3(*e*) disappear when the same small-amplitude random perturbation is employed; see Appendix A.3 for discussion of these random perturbation tests.

The fluctuation fields preserve their spatial structure at early times as their amplitudes grow exponentially. The vertical vorticity fluctuation $\omega'_z$ is plotted on the left-hand side of figure 5 for six values of $Fr_z$ between 0.1 and 3. It is shown at $z=0$, a maximum displacement level, where the amplitude of the vorticity perturbation is greatest. For $Fr_z < 1$ (figure 5*a–d*), the vorticity fluctuation closely resembles the linear eigenfunctions computed in Billant & Chomaz (2000*c*). It is characterized by a broad negative perturbation oriented along the $x$-axis, flanked by positive perturbations on either side in the $y$-direction (see figure 5*a* for terminology). This perturbation translates the Lamb–Chaplygin dipole in the positive $y$-direction and rotates it counter-clockwise with little change to its horizontal structure. As $Fr_z$ is increased to 0.628, the maxima of each of the positive perturbations move towards the front, while isolated minima appear behind them.

For shorter perturbations with $Fr_z > 1$ (figure 5*e*, *f*), the structure of the vorticity fluctuation is fundamentally different from that of the zigzag instability. The positive perturbations on each side of the vortex pair split in two, while the structure of the central minimum increases in complexity. The topology of these fluctuations

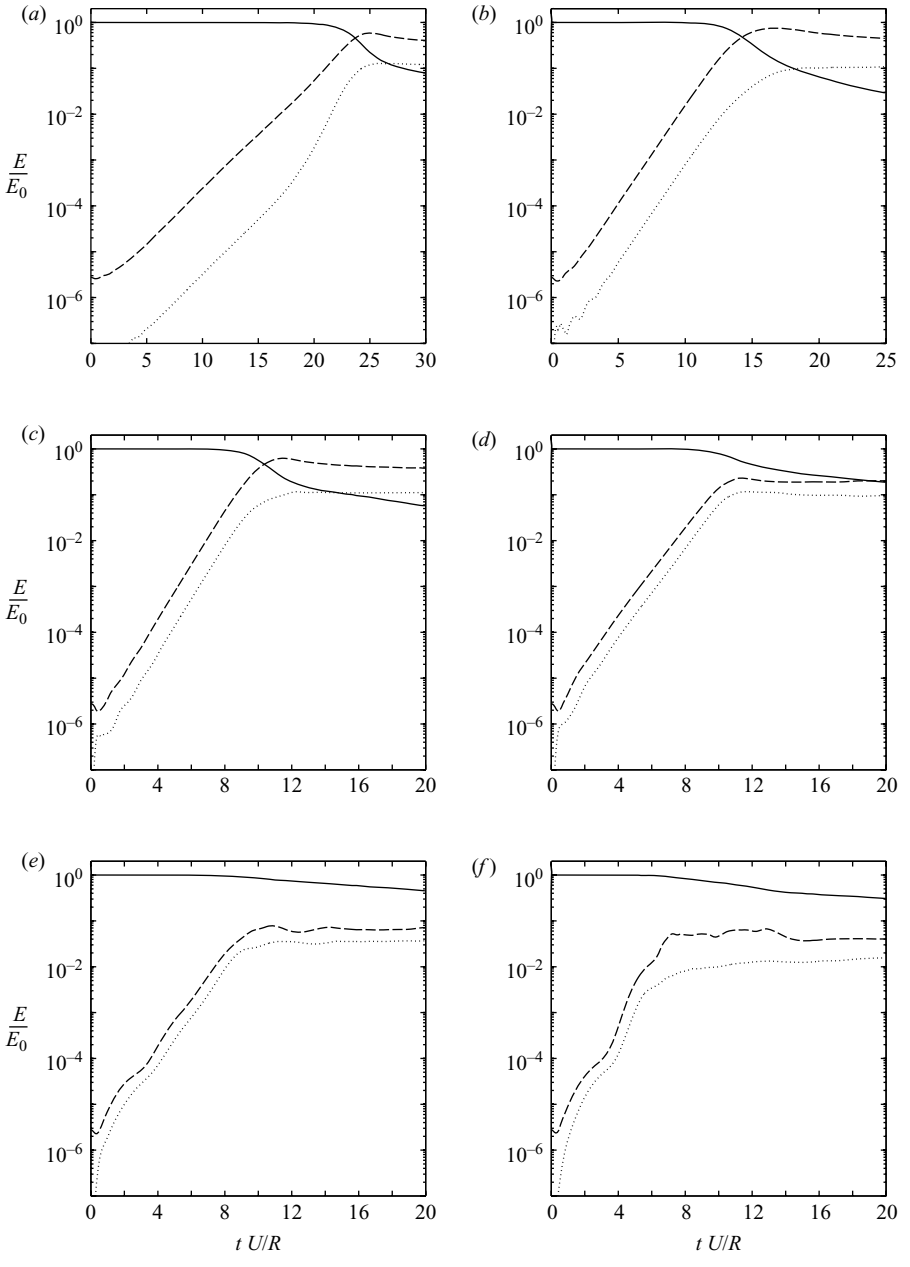


FIGURE 3. Time series of vertically averaged kinetic energy $\overline{E}_K$ (solid), fluctuation kinetic energy $E'_K$ (dashed) and fluctuation potential energy $E'_P$ (dotted) for $Fr_h = 0.1$ and $Fr_z = 0.157$ (*a*), 0.314 (*b*), 0.628 (*c*), 1.26 (*d*), 2.51 (*e*) and 5.02 (*f*). Energies are normalized by $\overline{E}_K(t = 0)$.

resembles that of the elliptic instability for the Lamb–Chaplygin dipole in the absence of stratification, though the fluctuations over the vortex cores are relatively weaker in the present case (cf. Billant *et al.* 1999, figure 4*a*). Though the elliptic instability is suppressed when $Fr_h < 0.2$, Miyazaki & Fukumoto (1992) found that related instabilities emerge at stronger stratifications for an unbounded strained vortex. These

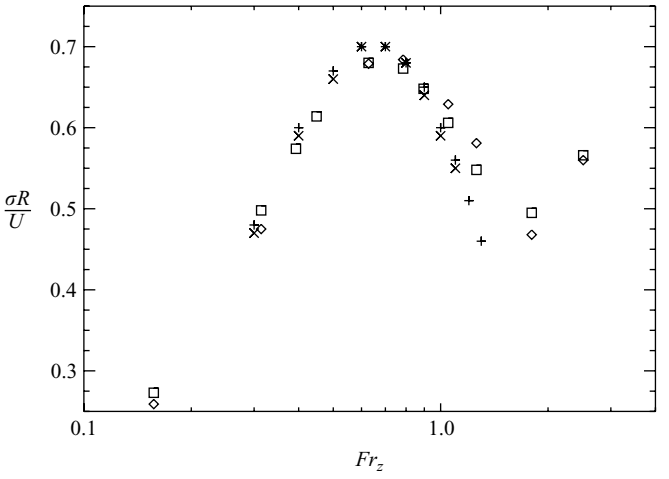


FIGURE 4. Dimensionless growth rate $\sigma R/U$ vs. $Fr_z$ for $Fr_h = 0.1$ ($\square$) and $Fr_h = 0.05$ ($\diamond$). We compute $\sigma$ by fitting the line $\sigma t + b$ to $\log E'_K/2$ over a time interval during which the growth is exponential: $4 \leqslant tU/R \leqslant 20$ for $Fr_z = 0.157$ and $4 \leqslant tU/R \leqslant 8$ for the others. Also shown are the growth rates computed in the linear simulations of Billant & Chomaz (2000*c*) for $Fr_h = 0.1$ (+) and $Fr_h = 0.05$ ($\times$) (after their figure 9).

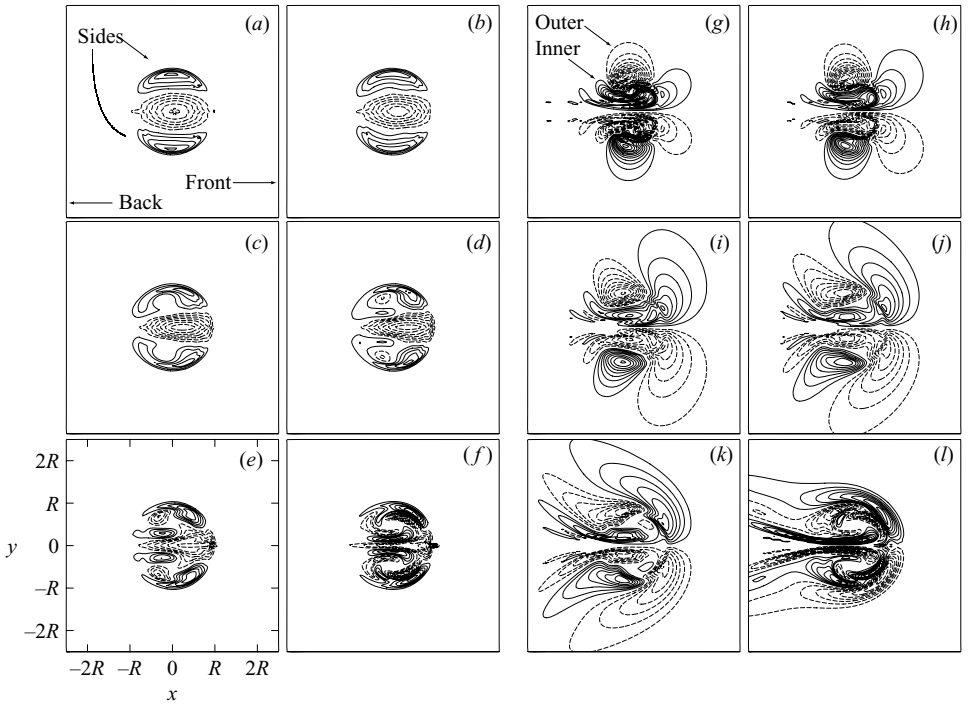


FIGURE 5. Horizontal $(x,y)$ slices of vertical vorticity fluctuation $\omega'_z$ (left two columns) and density $\rho$ (right two columns) for $Fr_h = 0.1$ and $Fr_z = 0.157$ $(a, g)$, 0.314 $(b, h)$, 0.628 $(c, i)$, 0.896 $(d, j)$, 1.26 $(e, k)$, and 2.51 $(f, l)$. Vorticity is displayed at the maximum displacement level $z = 0$ and density at the inflection level $z = \lambda_z/4$. All plots are at time $tU/R = 5$, are centred in $x$ on the vortex pair, and have the same $x,y$ scales. Fluctuation fields have been normalized by their root-mean-square values. Negative contours are dashed, and no zero contours are shown.

instabilities are driven by higher-order resonances between internal gravity waves and the oscillating strain field induced by the vortices. The instability we observe for $Fr_z > 1$ may be due to the analogous higher-order resonance for the vortex pair. A rigorous study of the stability of the Lamb–Chaplygin dipole, which has a much more complicated dispersion relation than the unbounded strained vortex considered by Miyazaki & Fukumoto (1992), would be required to investigate this hypothesis.

Density perturbations are plotted on the right side of figure 5 at $z = \lambda_z/4$, an inflection level, where they have maximum amplitude (the vorticity and density perturbations are $\pi/4$ out of phase). For $Fr_z < 1$ (figure 5*g–j*) there is a pair of opposite-signed perturbations on each side of the line of symmetry, which we call inner and outer. The inner perturbation is adjacent to the line of symmetry and spans its length, while the outer perturbation is centred over the sides (see figure 5*g*). As $Fr_z$ approaches unity, the leading edge of the inner perturbation broadens. A train of small-scale gravity waves (not mentioned in Billant & Chomaz 2000*b*, *c*) follows the vortex pair in all cases, but is most prominent for $Fr_z$ close to unity. As $Fr_z$ is increased above unity (figure 5*k*, *l*), the inner perturbation breaks into two, and a distinct pair of opposite-signed perturbations appears in the region of the split. The leading half of the inner perturbation narrows and is swept around the outer perturbation, while the trailing half extends far behind the vortex pair.

### 3.2. *Nonlinear regime*

The exponential growth of the linear regime ultimately gives way to nonlinear interactions and, as we shall see, the breakdown of the vortex pair into turbulence. The nature of this transition varies with $Fr_z$. In § 3.2.1 we discuss the fastest growing modes of the zigzag instability, which appear to share a common mechanism of transition to turbulence. Taller and shorter perturbations have more complicated nonlinear dynamics, and are discussed briefly in § 3.2.2 and § 3.2.3.

#### 3.2.1. *Dominant zigzag modes:* $0.3 < Fr_z < 0.8$

We begin by examining the nonlinear evolution of the nearly fastest growing perturbation with $Fr_z = 0.628$. Perturbations with $0.3 < Fr_z < 0.8$ behave similarly. Figure 6 shows the vertical vorticity evolution at the maximum displacement level $z = 0$ and inflection level $z = \lambda_z/4$. At early times the evolution agrees with the linear predictions: the dipole is relatively unchanged at the inflection level, and is slightly twisted and displaced at the maximum displacement level. The dipole structure eventually gives way to small-scale vorticity, showing the emergence of turbulence. This small-scale disturbance first appears at the inflection levels at time $9 \leqslant tU/R \leqslant 11$, and then at other levels by $tU/R = 13$. The maximum displacement of the dipole from its initial $y$-position appears to be less than $R$ at the onset of turbulence. This saturation amplitude is surprisingly low, considering that the laboratory dipoles of Billant & Chomaz (2000*a*) displaced several times $R$ without saturating. It will be shown in § 3.3 that this distinction is due to the lower Reynolds number of the laboratory experiments.

A three-dimensional visualization of the transition to turbulence is given in figures 7 and 8, which show the PV field (2.6) at $tU/R = 9$, 10, 11 and 12. The PV provides an ideal representation of the dipole because it is materially conserved in the absence of viscosity and diffusion (equation (2.7)). The Lamb–Chaplygin dipole has two vertical tubes of PV, which by $tU/R = 9$ are bent and twisted, in line with the linear zigzag instability theory (figures 7*a*, 8*a*). At $tU/R = 10$, a disturbance is visible on the interior edges of the vortices around the inflection levels (figure 8*b*); narrow horizontal

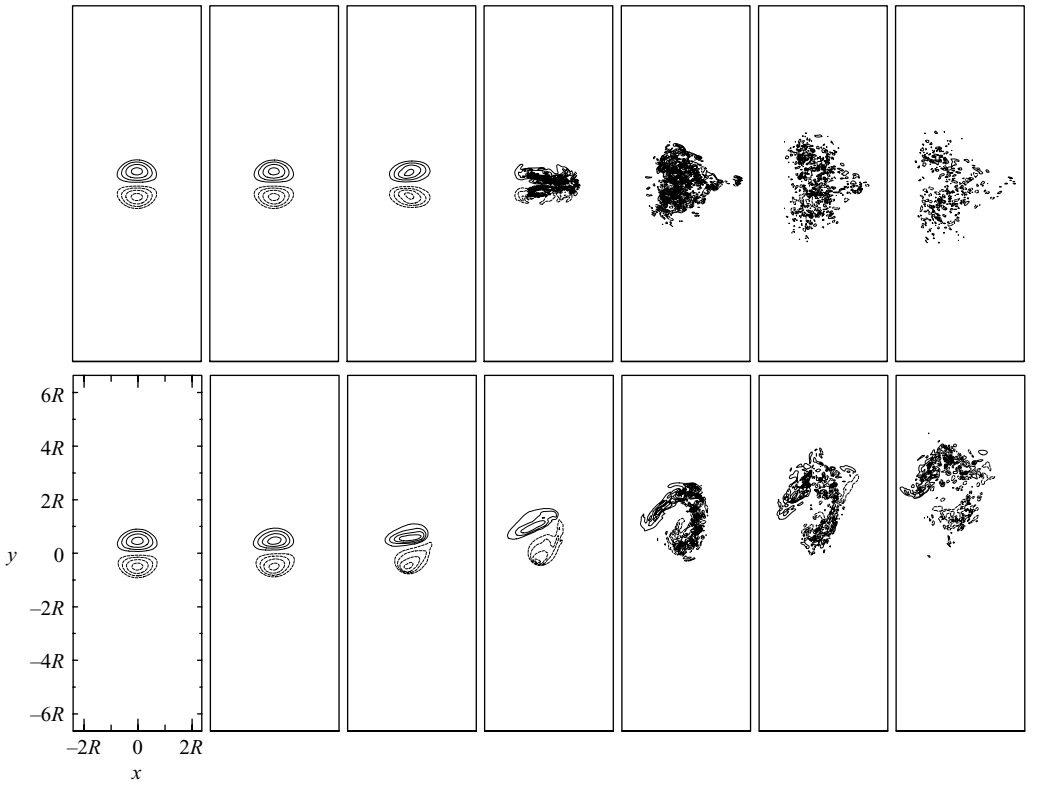


FIGURE 6. Horizontal $(x,y)$ slices of vertical vorticity $\omega_z$ at the inflection level $z=\lambda_z/4$ (top row) and maximum displacement level $z=0$ (bottom row) for $Fr_h=0.1$ and $Fr_z=0.628$ at $tU/R=$ (from left to right) 5, 7, 9, 11, 13, 15, 17. All plots are centred in $x$ on the vortex pair and have the same $x,y$ scales. Contour intervals are $2.5\,U/R$, negative contours are dashed, and no zero contours are shown.

filaments have also appeared around the vortices at the same levels (figure 7*b*). By $tU/R=11$ the dipole PV structure at the inflection levels has completely disappeared, replaced by small-scale filaments that increase in complexity at $tU/R=12$. The dipole structure persists at maximum displacement levels but by $tU/R=12$ has begun to break up there as well. Figure 8, like figure 6, indicates that the vortices break up first at the inflection levels. What is happening in these regions?

The evolution of the density field provides further insight. Figure 9 shows the evolution of the isopycnal (isosurface of total density $\overline{\rho}+\rho$) with equilibrium height at the inflection level $\lambda_z/4$. This isopycnal, along with that at $z=3\lambda_z/4$, has the greatest displacement in the linear zigzag theory. Indeed, at $tU/R=9$ (figure 9*a*) the displacement largely follows the linear prediction illustrated in figure 5(*i*): moving across the dipole in the direction of positive $y$, the isopycnal is displaced upward, downward, upward, and downward from its equilibrium height. Superimposed on these displacements are structures not accounted for by the linear theory. Particularly striking is the train of gravity waves located behind the dipole. These waves are approximately stationary in the frame moving with the vortices, and grow in amplitude as the instability grows. They appear to be excited and maintained by nonlinear interactions with the growing vortex instability. By $tU/R=10$ (figure 9*b*), a profound transition has occurred: the upward perturbation located past the dipole centre (in

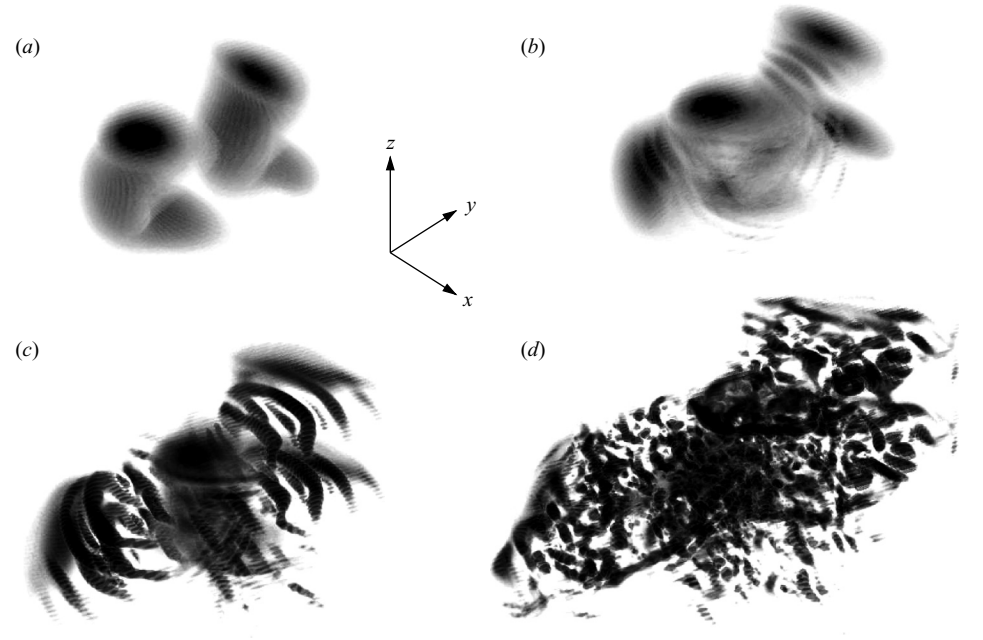


FIGURE 7. Three-dimensional visualization of PV magnitude for $Fr_h = 0.1$ and $Fr_z = 0.628$ at $tU/R = 9$ (*a*), 10 (*b*), 11 (*c*), and 12 (*d*). The view is from the direction of positive $x$, negative $y$, and positive $z$. Shading varies from white at $|\Pi| = \Pi_0/2$ to black for $|\Pi| \geqslant \Pi_0$, and opacity increases with $|\Pi|$. For clarity, values with $|\Pi| < \Pi_0/2$ are not plotted.

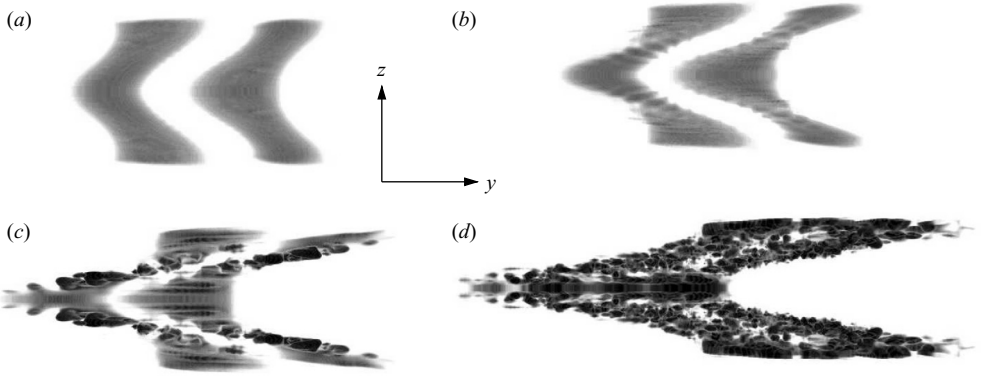


FIGURE 8. As in figure 7, but from the direction of the positive $x$-axis.

terms of $y$) has tipped over the neighbouring depression on the other side of the centreline, creating a gravitationally unstable region with $\mathrm{d}\overline{\rho}/\mathrm{d}z + \partial\rho/\partial z > 0$ (see also figures 19–21). The breakdown of the overturned isopycnal is co-located in time and space with the emergence of small-scale vorticity associated with the transition of the vortex pair to turbulence.

It can be shown that the onset of isopycnal overturning is consistent with the linear zigzag instability theory extended to finite amplitude. A basic property of the vortex-scaled dimensionless Boussinesq equations, on which the linear theory of Billant & Chomaz (2000*b*) is based, is that at lowest order in $Fr_h$ and $Fr_z$ the density is slaved

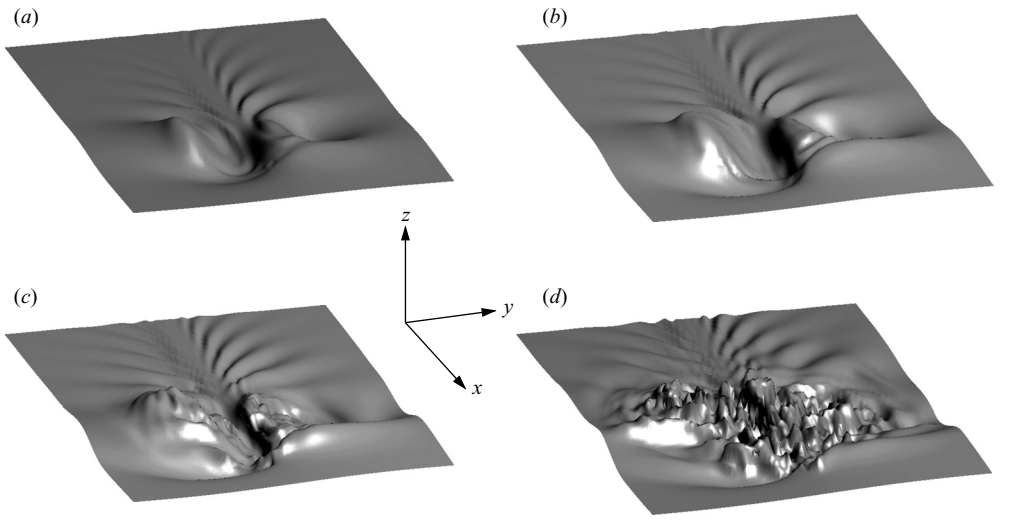


FIGURE 9. The isopycnal with equilibrium height at the inflection level $z = \lambda_z/4$ for $Fr_h = 0.1$ and $Fr_z = 0.628$ at $tU/R = 9$ (*a*), 10 (*b*), 11 (*c*), and 12 (*d*). The vertical coordinate has been stretched by a factor of four, exaggerating the isopycnal displacement for clarity. The surface has dimensions $4R \times 4R$.

to the velocity via hydrostatic balance (Drazin 1961; Riley *et al.* 1981; Lilly 1983). Specifically,

$$\nabla_h^2 \phi = -\nabla_h \cdot (\boldsymbol{u}_h \cdot \nabla_h \boldsymbol{u}_h)\,, \tag{3.5}$$

$$\frac{g}{\rho_0}\rho = -\frac{\partial \phi}{\partial z}\,. \tag{3.6}$$

In the linear theory, $\boldsymbol{u}_h$ is taken to be $\boldsymbol{u}_{h0}$ with an infinitesimal bend $\eta$ and twist $\psi$, i.e. $y_0$ in (2.3) is given by

$$y_0 = \eta \cos(k_z z), \tag{3.7}$$

and the dipole is rotated by an angle

$$\theta_0 = \psi \cos(k_z z). \tag{3.8}$$

Details of the twisting perturbation are given in Appendix B. The analysis then proceeds by linearizing around $\eta = 0$, $\psi = 0$ and determining the evolution of $\eta$ and $\psi$ on the slow time scales defined by $Fr_z$. In contrast, here we postulate that the vortex pair evolves via the zigzag instability to $\boldsymbol{u}_{h0}$ with a finite $\eta$ and $\psi$. This constrained evolution is a natural second approximation for early times when $\eta \lesssim R$. Indeed, it corresponds exactly to the lowest-order dynamics in an expansion in $Fr_h$, $Fr_z$. The resulting slaved density can be obtained by solving (3.5)–(3.6) with (2.4) and (3.7)–(3.8), which yield

$$\frac{g}{\rho_0}\rho = k_z U^2 \sin(k_z z)\,\left(\frac{\eta}{R} A(r/R, \theta, \theta_0) + \psi\, B(r/R, \theta)\right). \tag{3.9}$$

The dimensionless functions $A$ and $B$ are given in Appendix B.

A schematic of the bend-induced slaved density perturbation (3.9) is shown in figure 10 for the linear regime $\eta \ll R$ (figure 10*a*) and the finite-amplitude regime $\eta \sim R$ (figure 10*b*). The twist breaks symmetry in $x$ but does not qualitatively change this picture. The right-hand side of (3.9) depends on $z$ explicitly through $\sin(k_z z)$ and

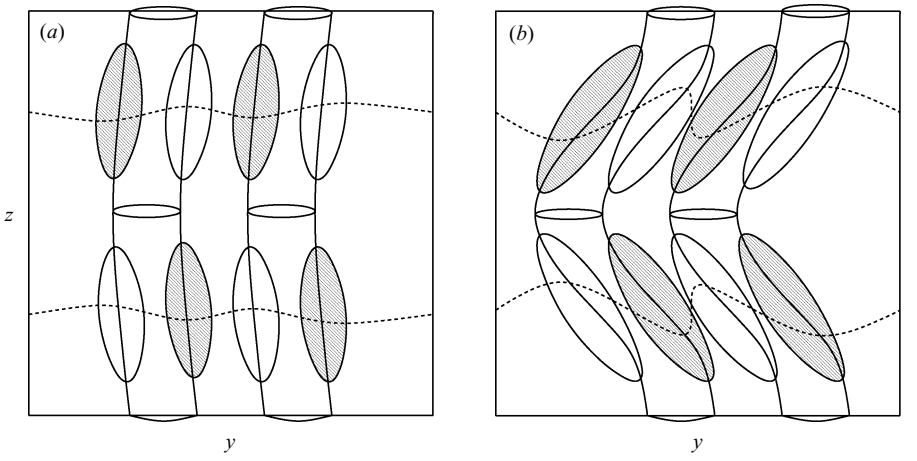


FIGURE 10. A schematic vertical $(y,z)$ slice through the centre of the dipole for $\eta \ll R$ $(a)$ and $\eta \sim R$ $(b)$. In both cases, $\psi$ is taken to be 0. The cylinders represent the vortex cores, the ellipses mark regions of positive (unshaded) and negative (shaded) density perturbation (3.9), and the dashed lines are isopycnals at the inflection levels.

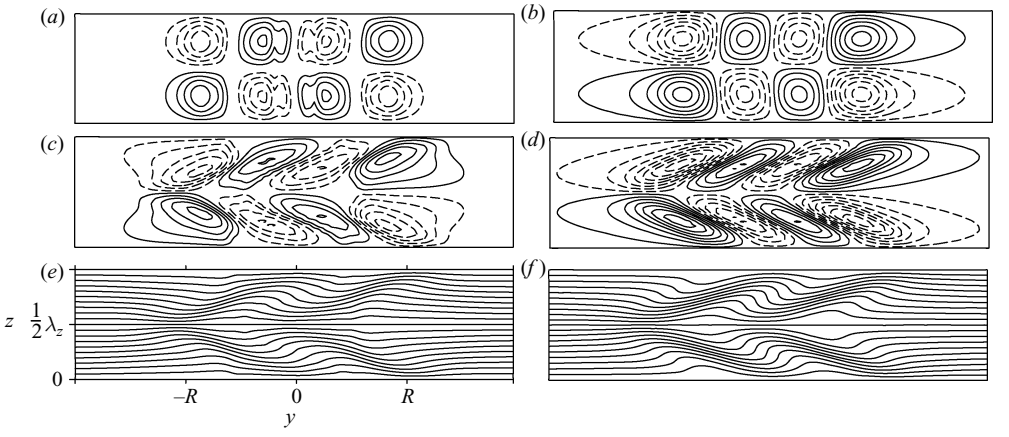


FIGURE 11. Vertical $(y,z)$ slices of density perturbation $\rho$ $(a–d)$ and total density $\overline{\rho}+\rho$ $(e, f)$. The left column shows simulation results for $Fr_h = 0.1$ and $Fr_z = 0.628$ at $tU/R = 5$ $(a)$ and $tU/R = 9.6$ $(c, e)$; the right column shows the corresponding analytical prediction (3.9) with $\eta/R = 0.013$, $\psi = 0.013$ $(b)$; and $\eta = 0.32$, $\psi = 0.28$ $(d, f)$. All plots are drawn through the centre of the dipole and have the same $y,z$ scales. Contour intervals are $0.0008\Delta\overline{\rho}$ (top), $0.016\Delta\overline{\rho}$ (middle), and $0.05\Delta\overline{\rho}$ (bottom), where $\Delta\overline{\rho} = -\mathrm{d}\overline{\rho}/\mathrm{d}z\,\lambda_z$. Negative contours are dashed, and no zero contours are shown.

implicitly through the variation (3.7), (3.8) of $y_0$ and $\theta_0$ with $z$. In the linear regime the former explicit contribution dominates. Billant & Chomaz (2000*b*) show that the resulting density perturbation forces a vertical velocity field that stretches the vortices at the maximum displacement levels and leads to exponential growth in $\eta$ (see their figure 4). At finite amplitude, the linear perturbation is bent and twisted significantly via (3.7), (3.8). Horizontal density gradients are tilted towards the vertical, resulting in isopycnal steepening at the inflection levels.

Figure 11 shows the simulation density at an early time $tU/R = 5$ and a later time $tU/R = 9.6$, immediately before the onset of overturning. The prediction (3.9) is also

plotted. For the latter, the bend $\eta$, twist $\psi$ and dipole centre $x_0$ are obtained by minimizing the difference between $\omega_z$ from the simulation and $\omega_{z0}$ (equation (2.5) with (3.7)–(3.8)) in a least-squares sense, yielding $\eta/R \approx 0.013$, $\psi \approx 0.013$ at $tU/R = 5$ and $\eta/R \approx 0.32$, $\psi \approx 0.28$ at $tU/R = 9.6$. The root-mean-square error of the fit is $O(0.1U/R)$. The simulation at both times is in qualitative agreement with (3.9), although the simulation density perturbations are slightly smaller than the analytical prediction. As suggested in figure 10, the bending and twisting of the slaved density field by finite $\eta$ produces large positive vertical gradients at the inflection levels; these gradients ultimately overturn the isopycnals.

The vertical derivative of (3.9) is

$$\frac{g}{\rho_0}\frac{\partial \rho}{\partial z} = k_z^2 U^2 \cos(k_z z)\left(\frac{\eta}{R}A + \psi B\right) + k_z^2 U^2 \sin^2(k_z z)\left(\left(\frac{\eta}{R}\right)^2 C + \frac{\eta}{R}\psi D + \psi^2 E\right), \quad (3.10)$$

where the functional dependence of $A, \ldots, E$ has been suppressed for clarity (see Appendix B). We can use (3.10) to determine the amplitude $\eta$ at which vertically oriented isopycnals will first appear. This occurs when $\mathrm{d}\overline{\rho}/\mathrm{d}z + \partial\rho/\partial z \geqslant 0$, i.e. when

$$\cos(k_z z)\left(\frac{\eta}{R}A + \psi B\right) + \sin^2(k_z z)\left(\left(\frac{\eta}{R}\right)^2 C + \frac{\eta}{R}\psi D + \psi^2 E\right) \geqslant Fr_z^{-2}. \quad (3.11)$$

The first (linear) term dominates when $\eta/R,\ \psi \ll 1$ and is the density gradient induced by the bend and twist in the linear zigzag theory. The second (nonlinear) term is a result of the finite-amplitude bending and twisting of (3.9).

The condition (3.11) has a complicated implicit dependence on $\eta$ and $\psi$ through the functions $A, \ldots, E$. We can simplify matters greatly by assuming that $\psi = 0$, i.e. considering the effect of the bend $\eta$ only. The maximum values of $A$ and $C$ are then 5.8 and 23, respectively (see Appendix B). In this case, the linear term predicts the onset of overturning at the maximum displacement levels when

$$\eta/R \approx 0.17/Fr_z^2, \quad (3.12)$$

which is large when $Fr_z$ is small; the nonlinear term therefore cannot be neglected. It is maximum at the inflection levels (where the linear term vanishes), and leads to overturning when

$$\eta/R \approx 0.21/Fr_z\,. \quad (3.13)$$

In figure 12($a$) we plot the values of $\eta/R$ at which overturning first appears in our simulations for $0.3 < Fr_z < 0.9$; $Fr_z = 0.157$ is omitted for reasons discussed in § 3.2.2 below. Overturning is determined to have occurred when $\mathrm{d}\overline{\rho}/\mathrm{d}z + \partial\rho/\partial z > 0$ at one or more grid points, with $\partial\rho/\partial z$ computed to an accuracy of $O(\Delta z^4)$. For $Fr_z < 0.8$, our results agree remarkably well with (3.13) (solid curve). The points in this range display a clear $Fr_z^{-1}$ scaling. The only exception is $Fr_z = 0.314$ and $Fr_h = 0.05$. In this case it appears that the large value of $\eta$ results in thin layers of reduced stratification that are poorly resolved by the vertical resolution employed; thus explicitly resolved overturning occurs at a later time and larger $\eta$ than for $Fr_h = 0.1$. For $Fr_z > 0.8$, the critical $\eta/R$ falls off faster than (3.13).

Neglecting the twist $\psi$ leads to the simple expression (3.13), the accuracy of which is seen in figure 12($a$) to degrade gradually as $Fr_z$ increases. Indeed, $\psi$ is non-negligible at the onset of overturning, with a value of around 0.3 for $0.3 < Fr_z < 0.8$ (figure 12$b$). When $\psi \neq 0$, the condition (3.11) is difficult to evaluate analytically. However, at fixed

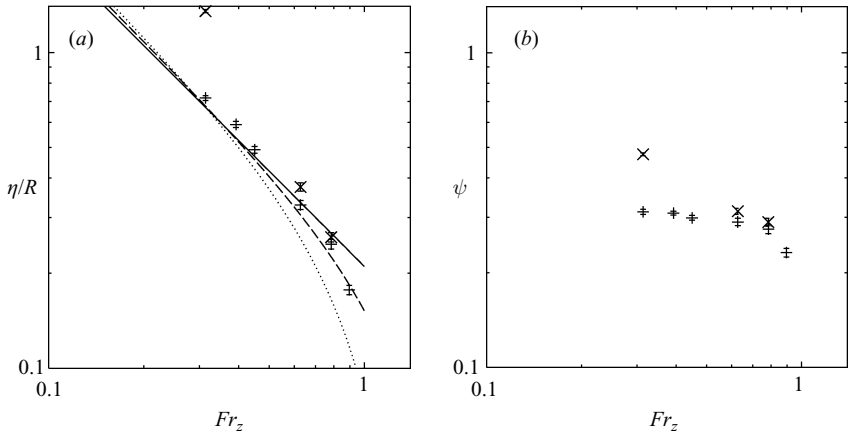


FIGURE 12. The normalized displacement amplitude $\eta/R$ (*a*) and rotation amplitude $\psi$ (*b*) at which overturning isopycnals first appear, for $0.1 < Fr_z < 0.9$ and $Fr_h = 0.1$ (+) and $Fr_h = 0.05$ (×). Error bars indicate the uncertainty due to the discrete times at which model output was analysed. The solid line in (*a*) is the analytical prediction $0.21 Fr_z^{-1}$ from (3.13), which assumes $\psi = 0$. Other lines show corresponding prediction for $\psi = 0.2$ (dashed) and 0.3 (dotted).

$\psi$ and $Fr_z$, we can compute numerically the smallest $\eta/R$ at which overturning at the inflection levels occurs. In figure 12(*a*) we plot these critical values for a selection of non-zero $\psi$. The curves collapse to (3.13) for $Fr_z < 0.6$, justifying our neglect of $\psi$ at small and moderate $Fr_z$. At larger $Fr_z$, inclusion of the twist accounts for the more rapid falling off of $\eta/R$ with $Fr_z$.

The reasoning that led to (3.11) appears to capture the basic dynamics of the simulations: the zigzag instability grows until the slaved density perturbations generated by the bending and twisting vortices overturn. Turbulence then results and rapidly dissipates the vortices. For $Fr_z < 0.6$, the twist has no significant effect on the breaking amplitude, and (3.13) gives a good prediction for the bend $\eta$ at which overturning occurs. For short perturbations with $Fr_z$ approaching unity, the agreement between (3.13) and the simulations is diminished. It is improved, however, when the bend $\psi$ is considered. Viscous effects, which were neglected in the derivation of (3.11), will certainly affect the transition to turbulence, and are discussed in § 3.3. However, given that the simulations in figure 12(*a*) have a finite, implicit Reynolds number, it appears that (3.11) applies at large finite $Re$. As $Fr_z$ surpasses unity, we expect the condition (3.11) to fail, since it assumes, as does the zigzag instability itself, small $Fr_z$. The prediction also fails, however, for tall perturbations with $Fr_z = 0.157$. We will examine these two exceptional cases next.

### 3.2.2. *Tall perturbations:* $Fr_z = 0.157$

Tall perturbations with $Fr_z = 0.157$ are well within the linear zigzag instability regime, but saturate differently than shorter zigzag modes. The growth rate at this $Fr_z$ is slow, less than half that of the fastest growing wavelengths. As the primary disturbance slowly grows, higher harmonics are able to attain significant amplitude. These shorter perturbations are initialized at low amplitude (see equation (2.10)) but have higher growth rates than the primary mode. By $tU/R = 23$, the fifth harmonic has grown to nearly dominate the disturbance, as can be seen in the PV field as well as the $k_z$ energy spectrum (figure 13). Turbulence sets in at a displacement $\eta$ comparable to (3.13) for $Fr_z = 5 \times 0.157$, and is localized around $z = \lambda_z/4$ and $3\lambda_z/4$.

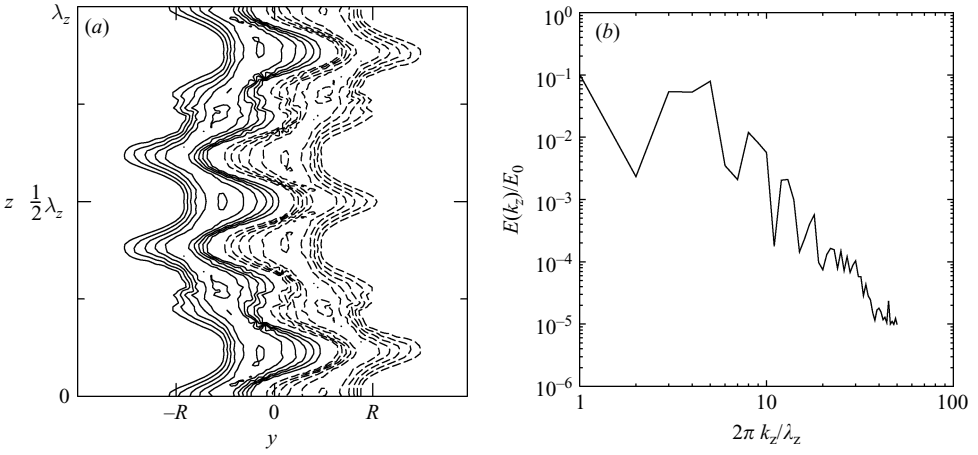


FIGURE 13. (*a*) Vertical ($y$,$z$) slices of PV for $Fr_h = 0.1$ and $Fr_z = 0.157$ when $tU/R = 23$. The plot is drawn through the centre of the dipole. Contour intervals are $\Pi_0/6$, negative contours are dashed, and no zero contours are shown. (*b*) The corresponding vertical wavenumber kinetic energy spectrum.

The initial transition to turbulence appears to be somewhat more complicated than the simple overturning of the fifth harmonic.

3.2.3. *Short perturbations: $Fr_z > 1$*

Short perturbations with $Fr_z > 1$ undergo a short-wave instability that is distinct from the zigzag instability, and so it is not surprising that their nonlinear dynamics are different as well. One of the most striking aspects of their behaviour can be seen in the time series of energy (figure 3). In the case of the zigzag instability ($Fr_z < 1$), the fluctuation kinetic energy $E'_K$ grows exponentially until it is nearly as large as the original vertically averaged energy $\overline{E}_K$. For $Fr_z > 1$, however, the instability saturates at a much lower amplitude. For $Fr_z > 2$, $E'_K$ peaks at an order of magnitude less than $\overline{E}_K$. The vertically averaged energy slowly decreases after the saturation of the instability. The vortex pair remains predominantly two-dimensional for many turnover times. Similar behaviour has been observed in unstratified flows with small aspect ratio (Ngan, Straub & Bartello 2005).

Figure 14 shows the vertical vorticity at $z = 0$ and $z = \lambda_z/4$ for $Fr_z = 2.51$. Unlike at smaller $Fr_z$, there is no apparent translation or twisting of the vortex pair. At $tU/R = 9$, a small-scale vorticity disturbance appears at the leading edge of the dipole. The isopycnals with equilibrium height at the inflection levels have overturned in this region (figure 15). The turbulence generated by this overturning appears to advect around the vortex cores without destroying them. Indeed, even at $tU/R = 17$, coherent cores are clearly visible in the vertical vorticity field (figure 14, right panels). Thus short perturbations, despite their significant growth rate, may have a less destructive effect on the vortex pair than taller perturbations. This may be expected given that short perturbations result in regions of overturning that are highly localized in space; taller perturbations, on the other hand, lead to overturning on the same scale as the dipole itself.

### 3.3. *Effects of reduced Reynolds number*

Viscosity can modify the evolution of the vortex pair fundamentally. In the linear regime, it reduces growth rates from their inviscid values (see Billant & Chomaz

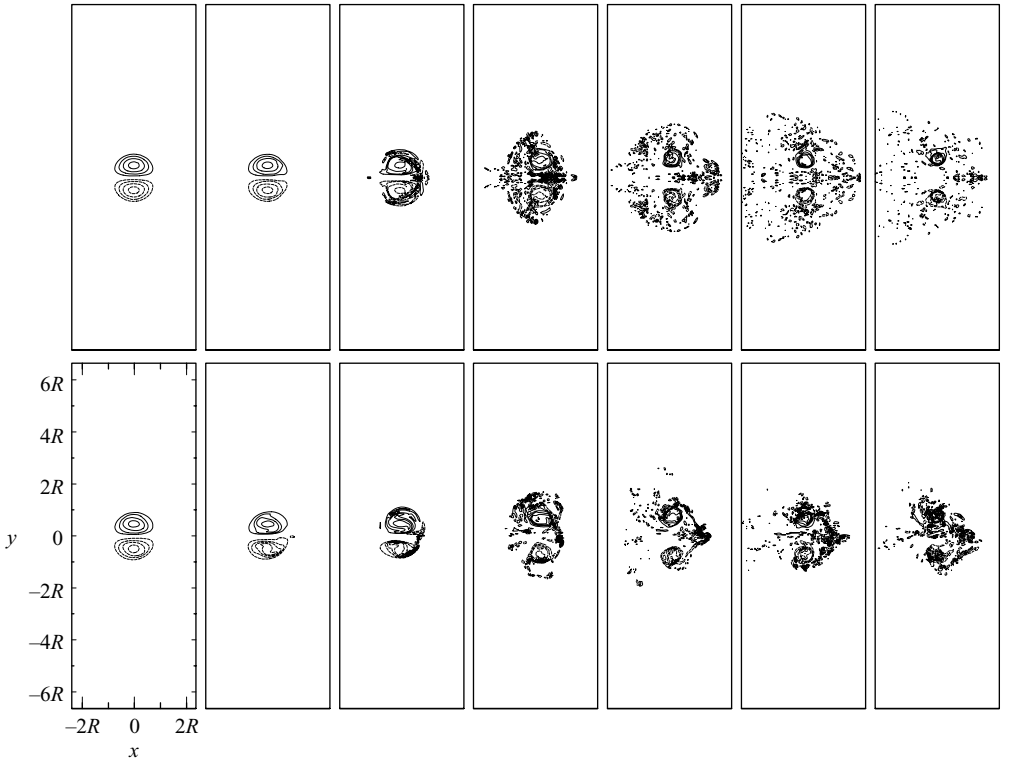


FIGURE 14. Horizontal $(x,y)$ slices of vertical vorticity $\omega_z$ at the inflection level $z=\lambda_z/4$ (top row) and maximum displacement level $z=0$ (bottom row) for $Fr_h=0.1$ and $Fr_z=2.51$ at $tU/R=$ (from left to right) 5, 7, 9, 11, 13, 15, 17. Other details are as in figure 6.

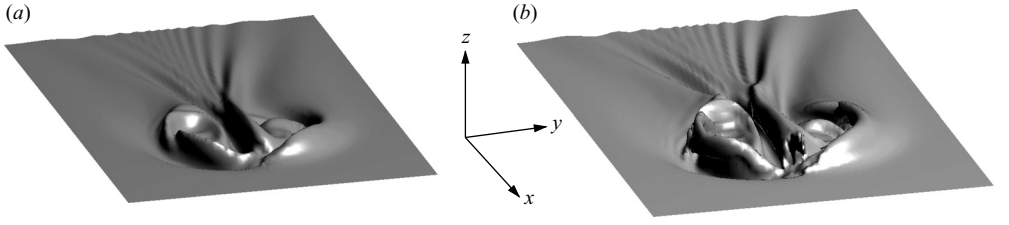


FIGURE 15. The isopycnal with equilibrium height at the inflection level $z=\lambda_z/4$ for $Fr_h=0.1$ and $Fr_z=2.51$ at $tU/R=8$ $(a)$ and 9 $(b)$. The vertical coordinate has been stretched by a factor of two, exaggerating the isopycnal displacement for clarity. Other details are as in figure 9.

2000 *c*). In the nonlinear regime, we have found that it can prevent isopycnals from overturning and breaking up into turbulence, and can lead to distinct laminar nonlinear dynamics. Here we investigate the viscous nonlinear evolution of the nearly fastest growing wavelength with $Fr_z=0.628$ at different $Fr_h$, $Re$, and $Sc$ (see table 2). The fastest growing modes at different $Fr_h$ have nearly identical inviscid growth rates but various vertical wavelengths, and thus will not necessarily respond in the same way to a given $Re$. Two Schmidt numbers are considered: $Sc=685$, representative of salt in water for comparison with laboratory experiments; and $Sc=1$. The viscous simulations with $Sc=685$ are quasi-DNS: the Kolmogorov scale $l_d\equiv(\nu^3/\epsilon)^{1/4}$ is

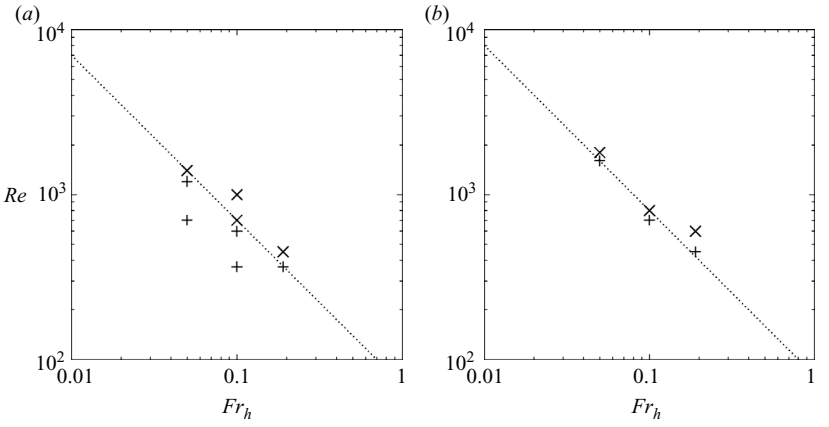


FIGURE 16. Simulations with non-zero $\nu$ plotted on the $Fr_h$–$Re$ plane, for $Sc = 685$ ($a$) and $Sc = 1$ ($b$). In all cases $Fr_z = 0.628$. Here $\times$ denotes a simulation in which isopycnals overturn; otherwise, $+$ is used. The dotted line in ($a$) is $70/Fr_h$ and in ($b$) is $80/Fr_h$. The $+$ at $Fr_h = 0.19$ in ($a$) corresponds closely with the laboratory experiment in figure 10 of Billant & Chomaz (2000$a$).

$O(\Delta x)$ (cf. Moin & Mahesh 1998), but the Batchelor scale $l_d Sc^{-1/2}$ is much smaller. Here $\epsilon$ is the maximum kinetic energy dissipation rate, computed from time series of average kinetic energy. The simulations with $Sc = 1$ are DNS for $Re < 1600$ and borderline LES at larger $Re$ (see Margolin *et al.* 2006$b$, for a discussion of the transition from DNS to implicit LES). The Kolmogorov scales for these simulations are given in table 2.

In the explicitly inviscid simulations of § 3.2.1, isopycnals ultimately overturn. With viscosity, our simulations show that there is a critical Reynolds number $Re_c$ below which overturning is inhibited and the flow remains laminar. Unless $Re$ is sufficiently larger than $Re_c$, overturning occurs at larger values of $\eta/R$ than those in figure 12($a$). From dimensional-analysis arguments, $Re_c$ can be expressed as a function of $Fr_z$ and $Fr_h$. With $Fr_z$ fixed at 0.628, $Re_c$ appears to be inversely proportional to $Fr_h$. This can be seen in figure 16, in which we plot the viscous simulations in the $Fr_h$–$Re$ plane, and distinguish those with overturning from those without. The boundary between these regimes scales approximately as $70/Fr_h$ for $Sc = 685$ and $80/Fr_h$ for $Sc = 1$. The dependence on $Sc$ is therefore rather weak. These findings are robust as simulations with doubled numerical resolution yield identical results; see Appendix A.2. Since $\lambda_z/R = 10\,Fr_h$ in these simulations, overturning at a given $Re$ requires sufficiently tall perturbations. Different criteria may hold at other $Fr_z$ due to their reduced growth rates. The laboratory experiment illustrated in figure 10 of Billant & Chomaz (2000$a$) has $Fr_z \approx 0.628$, $Fr_h \approx 0.19$, and $Re = 365$, and thus lies in the laminar regime, though it is fairly close to the transition at $Re_c$.

The nature of the laminar regime depends crucially on the vertical scale, even at fixed $Re$ and $Fr_z$. Consider perturbations with $Fr_z = 0.628$ at $Fr_h = 0.1$ ($\lambda_z/R = 1$) and 0.19 ($\lambda_z/R = 1.9$), each at $Re = 365$ and $Sc = 685$, representative of laboratory experiments (runs 21 and 23 in table 2). With the shorter perturbation, the vortex pair retains the zigzag structure of a columnar vortex with a sinusoidal displacement well into the dissipative regime; i.e. $\eta$ remains less than $R$ (figure 17$a$). With the taller perturbation, by contrast, the zigzag amplitude $\eta$ grows to exceed $R$, causing the vortex dipoles centred around $z = 0$ and $\lambda_z/2$ to detach from one another and form

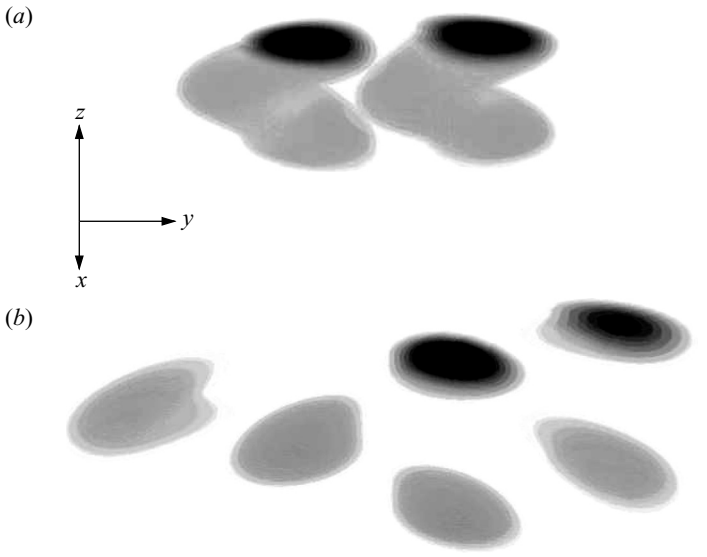


FIGURE 17. Three-dimensional visualization of PV magnitude for $Fr_z = 0.628$ and $Fr_h = 0.1$ (*a*), and $Fr_h = 0.19$ (*b*); with $Re = 365$ and $Sc = 385$. Both plots are at $tU/R = 40$, more than 10 turnover times after the maximum fluctuation kinetic energy is reached. The view is from above and ahead of the vortex pair. Shading varies from white at $|\Pi| = 0.1\Pi_{max}$ to black at $|\Pi| = \Pi_{max}$. For clarity, values with $|\Pi| < 0.1\Pi_{max}$ are not plotted.

pancake vortices (figure 17*b*) as observed in the laboratory (Billant & Chomaz 2000*a*). Interestingly, because of the $O(1)$ aspect ratio of the fastest growing wavelength at $Fr_h = 0.19$, the pancake vortices are more spherical than flat. Vertical decoupling occurs for narrow ranges of $Re$ and $\lambda_z/R$, small enough to suppress the transition to turbulence, but not so small as to inhibit the growth of $\eta$ to sufficiently large amplitude.

## 4. Conclusions

We have performed a series of numerical simulations of a counter-rotating vortex pair in a stably stratified fluid, and extended the linear analysis and laboratory experiments of Billant & Chomaz (2000*a*, *b*, *c*) to the fully nonlinear, large-$Re$ regime. The Lamb–Chaplygin vortex dipole, oriented parallel to a stable background vertical density gradient, was perturbed with a small-amplitude horizontal displacement that varies sinusoidally in the vertical. We have restricted our attention to strong stratifications with small $Fr_h < 0.2$, and a wide range of $Fr_z$, from tall perturbations with $Fr_z \approx 0.1$ to short with $Fr_z \approx 5$. While the evolution of small perturbations in our simulations agrees well with the linear predictions of Billant & Chomaz (2000 *b*, *c*), the finite-amplitude dynamics at large $Re$ are profoundly different from the moderate-$Re$ laboratory experiments of Billant & Chomaz (2000*a*).

Perturbations grow exponentially at early times. Tall disturbances with $Fr_z < 1$ behave as expected for the zigzag instability; their growth rates and structures agree well with the linear simulations of Billant & Chomaz (2000 *c*). In particular, the growth is most rapid at a vertical scale with $0.6 < Fr_z < 0.7$, independently of $Fr_h$. At short vertical scales with $Fr_z > 1$, a distinct instability exists: at $Fr_z = 2.5$ its growth rate is only 20% less than that of the fastest growing wavelength, so it can achieve

significant amplitude as the zigzag instability develops. Whether this growth rate has a non-zero limit as $Fr_z \to \infty$ is unclear from these results and requires further study. It is possible that this short-wave instability is the vortex pair analogue of the short-wave instability found by Miyazaki & Fukumoto (1992) in an unbounded strained vortex.

Eventually the linear instability gives way to nonlinear evolution, and at large Reynolds number this transition is characterized by the onset of turbulence. The major result of this work is that, in the neighbourhood of the fastest growing zigzag wavelength ($0.2 < Fr_z < 0.8$), this transition follows a common mechanism, which can be accounted for by the lowest-order dynamics of strongly stratified vortex motion. Density perturbations resembling those predicted by the linear theory (Billant & Chomaz 2000*b*) grow and are tilted by the finite-amplitude horizontal displacement of the vortices. The tilting of horizontal density gradients towards the vertical creates regions of reduced stratification at the inflection levels. Isopycnals ultimately overturn, resulting in gravitational instability and the breakdown into turbulence that destroy the vortex pair. An extension of the linear zigzag theory to finite amplitude indicates that overturning occurs when the horizontal displacement amplitude $\eta$ satisfies $\eta/R \approx 0.21/Fr_z$ for $Fr_z < 0.8$. As $Fr_z \to 1$, the twisting of the dipole leads to smaller critical values of $\eta/R$. Our simulations agree well with these predictions.

Viscosity inhibits the steepening of isopycnals and can suppress the transition to turbulence. For the nearly fastest growing wavelength with $Fr_z = 0.628$, the development of overturning requires $ReFr_h > 80$. The stabilizing effect of viscosity accounts for the discrepancy between our large-$Re$ simulations and the laboratory experiments of Billant & Chomaz (2000*a*), which remained laminar. In the laminar regime, decoupling of the vortices at different levels – with coherent pancake vortices that persist for long times – occurs only if the vertical scale is sufficiently large, but not large enough to allow overturning. The fact that these structures are maintained by viscosity suggests they have limited relevance for the large-$Re$ regime. Indeed, our study highlights the difficulty of extrapolating results from laboratory to geophysical Reynolds numbers, which differ by many orders of magnitude. The saturation mechanism of the zigzag instability is fundamentally distinct in these two regimes.

The short-wave instability evolves very differently from the zigzag instability, despite its comparable growth rate. It saturates at a much lower amplitude, with fluctuation kinetic energy around an order of magnitude less than that of the background columnar vortices. Turbulence results from the development of localized overturning at the leading edge of the vortex pair. However, unlike for the zigzag instability, the turbulence does not rapidly destroy the vortices, which are instead dissipated slowly and remain predominantly columnar for many turnover times. These short perturbations have small $\lambda_z/R$ (and large $Fr_z$), and their evolution is reminiscent of the instability of thin two-dimensional flows to three-dimensional perturbations in unstratified fluids (Ngan *et al.* 2005).

In this work, we have analysed the saturation of the zigzag instability of a counter-rotating columnar vortex pair perturbed at a distinct vertical scale, which may be a fundamental mechanism for the generation of turbulence in stratified fluids. A direct extension of this study would be to consider the nonlinear evolution of broadband random perturbations. Does the fastest growing zigzag wavelength dominate and develop as described in §3.2.1, or are interactions between different vertical scales important? A key issue is the potential interplay between the short-wave and zigzag instabilities. The low saturation amplitude of the short-wave instability suggests that

| Run | $Fr_h$ | $Fr_z$ | $\lambda_z/R$ | $\Delta z/\Delta x$ | $\lambda_z/\Delta z$ |
|---|---|---|---|---|---|
| 1b | 0.1 | 0.157 | 4 | 5 | 20 |
| 2b | 0.1 | 0.314 | 2 | 0.5 | 100 |
| 5b | 0.1 | 0.628 | 1 | 0.5 | 50 |
| 9b | 0.1 | 1.26 | 0.5 | 0.3125 | 40 |
| 11b | 0.1 | 2.51 | 0.25 | 0.15625 | 40 |
| 14b | 0.05 | 0.314 | 1 | 0.5 | 50 |

TABLE 3. Parameters used in the simulations testing sensitivity to vertical resolution. Run numbers correspond to the primary simulations in table 1.

its effect might be negligible. However, the turbulence it generates may modify the growth rate and nonlinear evolution of the zigzag instability to an unknown degree. Indeed, preliminary results suggest that the saturating short-wave instability can damp the growth of the zigzag modes, but more investigation is required.

Equally intriguing is the question of how the zigzag instability and its tendency to break down into turbulence might apply to more general vortex structures. It is plausible that vortices with a finite vertical scale $H \gtrsim O(U/N)$ might be subject to the same basic instability mechanism at large Rossby number $Ro = \omega_z/f$, where $f$ is the Coriolis parameter characterizing the Earth's rotation. Our results suggest that such vortices would not only develop vertical scales of $O(U/N)$, but would be subsequently dissipated by turbulence. Additionally, a recent study by Deloncle, Billant & Chomaz (2008), of which the authors became aware after the completion of this work, suggests that the horizontal structure of the vortex pair influences the nature of the transition to turbulence. They found that a pair of counter-rotating Gaussian vortices, which have greater separation than those in the Lamb-Chaplygin dipole, undergoes a Kelvin–Helmholtz instability for $Re\,Fr_h^2 > 340$. This criterion is distinct from our overturning condition $Re\,Fr_h > 80$. Clearly, the generalization of the zigzag instability and its nonlinear dynamics to a wider class of vortices warrants further study.

We would like to thank Peter Bartello, Paul Billant, Richard Rotunno, and two anonymous referees for helpful comments on the manuscript. M. L. W. gratefully acknowledges the support of the NCAR Advanced Study Program. P. K. S. acknowledges partial support from the Department of Energy (DOE) Climate Change Prediction Program (CCPP). Figures 7, 8 and 17 were created with the VAPOR visualization package (Clyne & Rast 2005). Computer time was provided by NSF MRI Grant CNS-0421498, NSF MRI Grant CNS-0420873, NSF MRI Grant CNS-0420985, NSF sponsorship of the National Center for Atmospheric Research, the University of Colorado, and a grant from the IBM Shared University Research (SUR) program. The National Center for Atmospheric Research is sponsored by the National Science Foundation.

## Appendix A. Sensitivity tests to model set-up and numerics

### A.1. *Vertical resolution*

Given the wide range of $\lambda_z$ considered, we have employed different vertical grid spacings in some of our simulations. We have therefore examined the sensitivity of our results to $\lambda_z/\Delta z$ (see table 3). Decreasing the resolution of the tallest perturbation

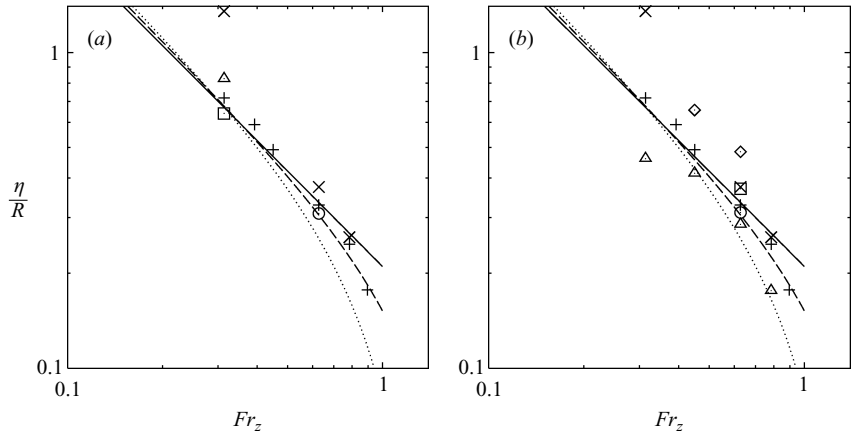


FIGURE 18. As in figure 12(*a*) with additional points representing sensitivity tests in Appendix A.1 (*a*) and A.2 (*b*). In (*a*), vertical resolution sensitivity tests are included: runs 2b (□), 5b (○) and 14b (△) from table 3. In (*b*), we plot results from the spectral transform model at medium (□) and high (○) resolution, the TKE model at medium resolution (◇), and EULAG at high-resolution (△).

$Fr_z = 0.157$ from $\lambda_z/\Delta z = 100$ to $\lambda_z/\Delta z = 20$ yields little change to the linear growth rate, but does modify the nonlinear evolution. Twenty grid points in the vertical therefore appear sufficient to reproduce the linear dynamics of the zigzag instability. Likewise, increasing $\lambda_z/\Delta z$ at other $Fr_z$ has a negligible effect on the linear growth rate.

Changes to the nonlinear regime are consistent with changes to the range of resolved scales. The transition to turbulence is naturally better resolved at higher resolution, but the basic mechanism of this transition remains the same. Simulations with $Fr_z < 0.8$, which have $\lambda_z/\Delta z > 20$, have a finer resolution of the turbulent regime than simulations with $Fr_z > 0.8$. The critical value of $\eta$ at which overturning appears is slightly reduced upon a doubling of vertical resolution (see figure 18*a*). This decrease is a consequence of the finite difference approximation to the overturning criterion as well as the increased effective Reynolds number.

### A.2. *Three-dimensional resolution and computational model*

Here we briefly demonstrate that the simulations described in this work are adequately converged with respect to spatial resolution, and moreover that similar results are obtained with a different computational model. We focus on the case of the most rapidly growing zigzag instability wavelength with $Fr_h = 0.1$ and $Fr_z = 0.628$ (run 5 in table 1). We use a smaller domain size than for our primary simulations in § 3, with $L_x = L_y = 8R$ and $L_z = \lambda_z$. Three resolutions are considered: the basic resolution employed in § 3 and summarized in table 1 (intermediate), one twice as coarse (low), and another twice as fine (high); see table 4.

Simulations are performed at each resolution with the non-oscillatory finite-volume model EULAG described in § 2.2 and a spectral-transform model (ST). ST uses third-order Adams–Bashforth time discretization together with fourth-order hyperviscosity and hyperdiffusion, i.e. the diabatic terms in (2.1) are replaced with $-\nu_8\nabla^8\boldsymbol{u}$ and $-\kappa_8\nabla^8\rho$. Coefficients are set to $\nu_8 \equiv \kappa_8 \equiv 0.5\Delta x^8$, which is just large enough to eliminate unphysical vorticity disturbances of scale $2\Delta x$. EULAG is run without explicit viscosity or diffusion. Note that for a given resolution, the grid spacing in ST

| | EULAG | | | | ST | | | |
|---|---|---|---|---|---|---|---|---|
| | $\Delta x/R$ | $\Delta z/\Delta x$ | $n \times m \times l$ | $\sigma R/U$ | $\Delta x/R$ | $\Delta z/\Delta x$ | $n \times m \times l$ | $\sigma R/U$ |
| Low | 0.08 | 0.962 | $100^2 \times 13$ | 0.633 | 0.0533 | 0.937 | $150^2 \times 20$ | 0.698 |
| Intermediate | 0.04 | 1 | $200^2 \times 25$ | 0.699 | 0.0267 | 0.937 | $300^2 \times 40$ | 0.711 |
| High | 0.02 | 1 | $400^2 \times 50$ | 0.711 | 0.0133 | 0.937 | $600^2 \times 80$ | 0.711 |

TABLE 4. Grid spacings and numbers of grid points employed by EULAG and ST for low, intermediate, and high resolutions. The growth rate $\sigma$, measured over $4 \leqslant tU/R \leqslant 8$ as in figure 4, is also given.

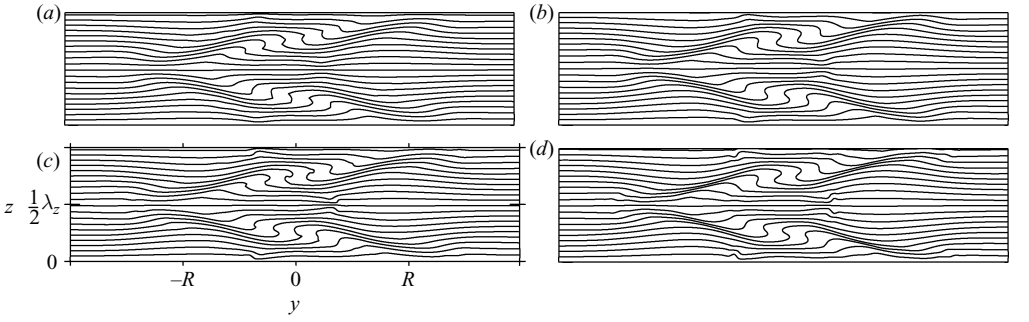


FIGURE 19. Vertical $(y, z)$ slices of total density $\overline{\rho} + \rho$ at $tU/R = 10$ with intermediate $(a, b)$ and high $(c, d)$ resolution obtained with EULAG $(a, c)$ and ST $(b, d)$. All plots are drawn through the centre of the dipole and have the same $y, z$ scales. Contour intervals are $0.05\Delta\overline{\rho}$.

is 2/3 smaller than that in EULAG. The high wavenumbers associated with this finer grid spacing are truncated after computing the nonlinear term to eliminate aliasing. Thus both models have the same number of degrees of freedom at a given resolution. The vertical grid spacing $\Delta z$ is set to $\Delta x$, or slightly less when necessary to ensure that the number of vertical grid points is an integer (or in the case of the ST, a product of small primes). The EULAG time step is chosen such that $\Delta t U/\Delta x = 0.125$. For ST, $\Delta t$ must be set to half the EULAG value to ensure stability.

The growth rates $\sigma$ of the linear regime are given in table 4. They converge at high resolution to $\sigma U/R = 0.711$ for both models. At intermediate resolution the EULAG value is within 2% of the converged value, and so this resolution accurately reproduces the mechanism of the zigzag linear instability. In the nonlinear regime there is a greater dependence on resolution and numerical method. This sensitivity is to be expected, since the transition to turbulence involves the excitation of a wide range of length scales. Increasing the resolution extends the range of resolved scales, while the two numerical models parameterize the effects of unresolved scales differently: EULAG implicitly through the truncation terms, and ST explicitly through hyperviscosity. The important question is whether the dynamics described in § 3, particularly the transition to turbulence via overturning isopycnals at the inflection levels, are robust.

To consider this question, we examine the density field after the appearance of gravitationally unstable isopycnals. Figure 19 shows the total density at $tU/R = 10$ at intermediate and high resolution for both models. Unstable isopycnals have appeared but not yet collapsed, and there is good agreement between the different models and different resolutions. At $tU/R = 11$, EULAG and ST agree qualitatively at high

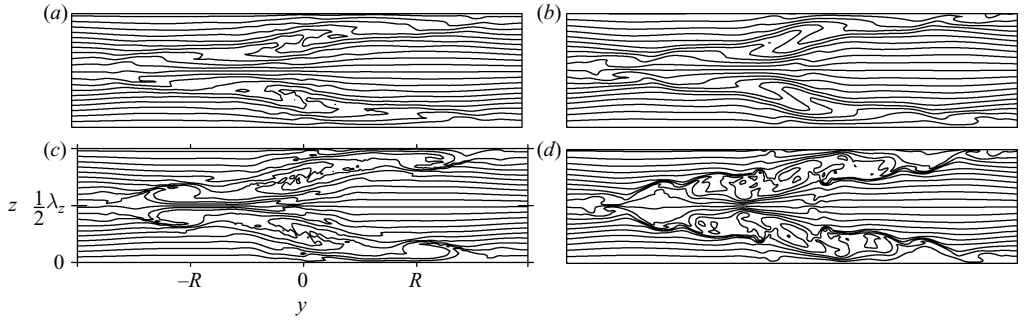


FIGURE 20. As in figure 19 but at $tU/R = 11$.

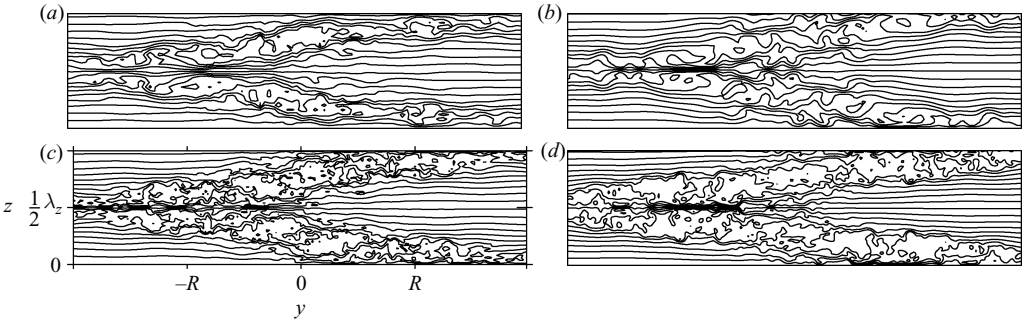


FIGURE 21. As in figure 19 but at $tU/R = 12$.

resolution. At intermediate resolution there are discrepancies with both models. EULAG successfully reproduces the development of small-scale disturbances on the overturned isopycnals associated with gravitational instability; density perturbations at the maximum displacement levels, however, are slightly suppressed relative to the high-resolution simulations (figure 20*a*). ST fails to capture the growing secondary instabilities in the regions of overturning (figure 20*b*). By $tU/R = 12$, the gravitational instability has fully transitioned to turbulence at intermediate and high resolution with both models. The formulation employed in § 3 (EULAG at intermediate resolution) reproduces this transition to turbulence in a way that closely resembles the high-resolution dynamics. While higher resolution gives a better reproduction of the turbulence generated after the collapse of the isopycnals, the conclusions of our study are unchanged. This agreement underlines the value of the ILES approach exploited by this study.

In figure 18(*b*), we plot the critical $\eta$ at which overturning occurs from the medium- and high-resolution ST simulations, superimposed on the values from figure 12(*a*). We also include the result from the high-resolution EULAG simulation discussed above, along with others at different $Fr_z$ with $Fr_h = 0.1$. ST and EULAG give similar critical $\eta$ at a given resolution, with the ST value slightly larger. The high-resolution EULAG results are consistently smaller than their medium-resolution counterparts discussed in § 3.2.1. This reduction in the value of $\eta$ at the onset of overturning is consistent with the finite difference approximation to the overturning criterion as well as the increased effective Reynolds number at higher resolution (see § 3.3). In the neighbourhood of the fastest growing mode ($0.4 < Fr_z < 1$), the decrease in $\eta$ is small, and the scaling and agreement with (3.11) is preserved.

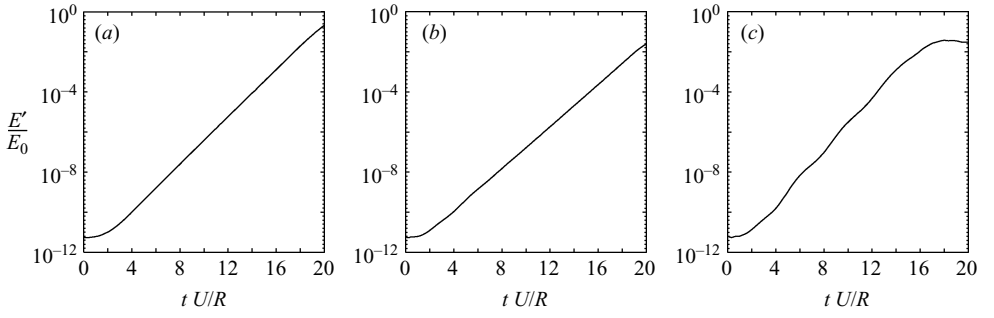


FIGURE 22. Time series of fluctuation kinetic energy $E'_K$ using random velocity perturbations at a single vertical wavelength, for $Fr_h = 0.1$ and $Fr_z = 0.628$ (*a*), 2.51 (*b*), and 5.02 (*c*). Energies are normalized by $\overline{E}_K(t=0)$.

For an additional point of comparison, we have performed simulations at $Fr_h = 0.1$ with an oscillatory finite difference scheme, employing second-order Adams–Bashforth time stepping and centred spatial discretization. These simulations are explicit LES, with the subgrid model implemented with a turbulent kinetic energy (TKE) approach (Schumann 1991). The resulting flow is significantly more dissipative than the ILES results described above. Nevertheless, the basic evolution is qualitatively unchanged: the zigzag instability grows until isopycnals overturn, then decays. The critical $\eta$ values associated with overturning are shown in figure 18(*b*). They are larger than the corresponding EULAG values, consistent with these having a lower effective Reynolds number.

We have also performed high-resolution sensitivity tests in the viscous regime. Following the same approach as described above for high-resolution EULAG in table 4, we have repeated simulations with $Fr_h = 0.1$ and $Fr_z = 0.628$ for four different ($Re$, $Sc$) combinations (runs 24, 25, 32, and 33). The existence of overturning is a binary result – either there is overturning or there is not – for which our high-resolution simulations agree exactly with the standard resolution runs in figure 16. For $Sc = 1$, overturning occurs for $Re = 800$ but not 700; for $Sc = 685$, overturning occurs for $Re = 700$ but not 600.

### A.3. *Initial perturbation*

The time series in figure 3 exhibit small deviations from exponential growth for $Fr_z > 2$. To verify the robustness of the results described in § 3 to the form of the initial perturbation, we have performed additional simulations with random perturbations. To the initial Lamb-Chaplygin velocity field, we add a non-divergent random perturbation at a single vertical wavelength. The velocity perturbations at each grid point are uniformly distributed between $\pm 10^{-6}\,U$. We have performed three such simulations, with $Fr_h = 0.1$ and $Fr_z = 0.628$, 2.51 and 5.02.

Time series of fluctuation kinetic energy are shown in figure 22. For $Fr_z = 0.628$ and 2.51, the growth is exponential, with growth rates (computed over $t = 5$–15) close to those shown in figure 4: within 0.3% for $Fr_z = 0.628$ and 6% for $Fr_z = 2.51$. Notably, the small deviations from exponential growth for $Fr_z = 2.51$ seen in figure 3(*e*) are suppressed. On the other hand, the time series for $Fr_z = 5.02$ display oscillations similar to those seen in figure 3(*f*). This behaviour is thus not a transient response to the form of the perturbation (2.9), but is consistent with the excitation of an unstable oscillatory mode.

## Appendix B. Finite-amplitude perturbations

The analysis in § 3.2.1 follows Billant & Chomaz (2000*b*) and is based on the vortex-scaled Boussinesq equations (Drazin 1961; Riley *et al.* 1981; Lilly 1983):

$$\frac{\partial \boldsymbol{u}_h}{\partial t} + \boldsymbol{u}_h \cdot \nabla_h \boldsymbol{u}_h + Fr_z^2\, w \frac{\partial \boldsymbol{u}_h}{\partial z} = -\nabla_h \phi, \tag{B 1a}$$

$$Fr_h^2 \left( \frac{\partial w}{\partial t} + \boldsymbol{u}_h \cdot \nabla_h w + Fr_z^2\, w \frac{\partial w}{\partial z} \right) = -\frac{\partial \phi}{\partial z} - \rho, \tag{B 1b}$$

$$\nabla_h \cdot \boldsymbol{u} + Fr_z^2 \frac{\partial w}{\partial z} = 0, \tag{B 1c}$$

$$\frac{\partial \rho}{\partial t} + \boldsymbol{u}_h \cdot \nabla_h \rho + Fr_z^2\, w \frac{\partial \rho}{\partial z} - w = 0\,. \tag{B 1d}$$

All variables in this Appendix have been non-dimensionalized with horizontal length scale $R$, vertical length scale $1/k_z$, horizontal velocity scale $U$, pressure scale $U^2$, and density scale $\rho_0 U^2 k_z/g$. The $*$ notation employed in (2.10) has been omitted for clarity. At lowest order in $Fr_h$ and $Fr_z$, $\rho$ is slaved to $\boldsymbol{u}_h$ through

$$\nabla_h^2 \phi = -\nabla_h \cdot (\boldsymbol{u}_h \cdot \nabla_h \boldsymbol{u}_h)\,, \tag{B 2}$$

$$\rho = -\frac{\partial \phi}{\partial z}\,. \tag{B 3}$$

The dimensionless Lamb–Chaplygin stream function, rotated by an angle $\theta_0$ and expressed in the rotated frame moving with unit velocity in the direction of the unrotated $x$-axis, is $S = S_0 + S_1$, where

$$S_0 = \begin{cases} \dfrac{-2}{\mu_1 J_0(\mu_1)} J_1(\mu_1 r) \sin\theta, & r \leqslant 1, \\ -r\left(1 - \dfrac{1}{r^2}\right) \sin\theta, & r > 1, \end{cases} \tag{B 4}$$

$$S_1 = -r\cos(\theta - \theta_0)\, \sin\theta_0 - r\sin(\theta - \theta_0)\,(\cos\theta_0 - 1), \tag{B 5}$$

$$x - x_0 = r\cos(\theta - \theta_0), \quad y - y_0 = r\sin(\theta - \theta_0), \tag{B 6}$$

and

$$\frac{\mathrm{d}x_0}{\mathrm{d}t} = -(\cos\theta_0 - 1), \quad \frac{\mathrm{d}y_0}{\mathrm{d}t} = \sin\theta_0. \tag{B 7}$$

Our aim is to determine $\rho$ when $x_0$ is constant and

$$y_0 = \eta\cos z, \quad \theta_0 = \psi\cos z, \tag{B 8}$$

i.e. the slaved density imposed by a single bending mode and twisting mode. The bent and twisted vortex pair (B 4) with (B 8) is an exact solution to (B 1) at lowest order in $Fr_h$ and $Fr_z$.

Equation (B 2) with $\boldsymbol{u}_h = \nabla \times (S\hat{\boldsymbol{e}}_3)$ can be written as

$$\nabla_h^2 \phi = \frac{1}{r}\frac{\partial}{\partial r}\left( r \nabla_h^2 S \frac{\partial S}{\partial r} \right) + \frac{1}{r^2}\frac{\partial}{\partial \theta}\left( \nabla_h^2 S \frac{\partial S}{\partial \theta} \right) - \frac{1}{2}\nabla_h^2 q^2, \tag{B 9}$$

where

$$q^2 = \left( \frac{\partial S}{\partial r} \right)^2 + \left( \frac{1}{r}\frac{\partial S}{\partial \theta} \right)^2. \tag{B 10}$$

A particular solution to (B 9) is

$$-\frac{J_0(\mu_1)}{2}\phi = \left(J_0^2(\mu_1 r) + J_1^2(\mu_1 r) - \frac{2}{\mu_1 r} J_0(\mu_1 r) J_1(\mu_1 r)\right) \sin^2\theta + \frac{1}{\mu_1^2 r^2} J_1^2(\mu_1 r), \tag{B 11a}$$

for $r \leqslant 1$, and

$$\phi = -\frac{1}{2}\left(1 + \frac{1}{r^2}\right)^2 + \frac{2}{r^2}\cos^2\theta, \tag{B 11b}$$

for $r > 1$. To within an additive constant, (B11) is the unique bounded solution to (B 9) on the plane.

The dependence of $\phi$ on $z$ is through (B 8), so both $r$ and $\theta$ are functions of $z$, with

$$\frac{\partial r}{\partial z} = \eta \sin z \sin(\theta - \theta_0), \tag{B 12}$$

$$\frac{\partial \theta}{\partial z} = \eta \sin z \frac{\cos(\theta - \theta_0)}{r} + \psi \sin z. \tag{B 13}$$

It follows that

$$\rho = -\frac{\partial \phi}{\partial z} = \eta \sin z\, A(r, \theta, \theta_0) + \psi \sin z\, B(r, \theta), \tag{B 14}$$

where

$$A(r, \theta, \theta_0) = -\left(\sin(\theta - \theta_0)\frac{\partial \phi}{\partial r} + \frac{\cos(\theta - \theta_0)}{r}\frac{\partial \phi}{\partial \theta}\right), \tag{B 15}$$

$$B(r, \theta) = -\frac{\partial \phi}{\partial \theta}. \tag{B 16}$$

Note that $A$ has an explicit dependence on the rotation angle $\theta_0$, in addition to the implicit dependence through $r$ and $\theta$. The functions $A$ and $B$ are given by

$$A(r, \theta, \theta_0) = \begin{cases} \dfrac{1}{J_0^2(\mu_1)}\dfrac{2}{r} A_1(r, \theta, \theta_0), & r \leqslant 1, \\ -\dfrac{2}{r^3}\left(\dfrac{1}{r^2}\sin(\theta - \theta_0) - \sin(3\theta - \theta_0)\right), & r > 1, \end{cases} \tag{B 17}$$

where

$$A_1(r, \theta, \theta_0) = J_1^2(\mu_1 r)\cos(\theta - \theta_0)\sin 2\theta - J_2^2(\mu_1 r)\sin(\theta - \theta_0) - J_0(\mu_1 r) J_2(\mu_1 r)\sin(3\theta - \theta_0);$$

and

$$B(r, \theta) = \begin{cases} \dfrac{2}{J_0^2(\mu_1)} B_1(r, \theta)\sin 2\theta, & r \leqslant 1, \\ \dfrac{2}{r}\sin 2\theta, & r > 1, \end{cases} \tag{B 18}$$

where

$$B_1(r, \theta) = J_0^2(\mu_1 r) - \frac{2}{\mu_1 r} J_0(\mu_1 r) J_1(\mu_1 r) + J_1^2(\mu_1 r).$$

The vertical density gradient is therefore

$$\frac{\partial \rho}{\partial z} = \cos z\,(\eta\, A(r,\theta,\theta_0) + \psi\, B(r,\theta)) + \sin z \left(\eta\, \frac{\partial A}{\partial z} + \psi\, \frac{\partial B}{\partial z}\right), \tag{B 19}$$

which has the form

$$\frac{\partial \rho}{\partial z} = \cos z\,(\eta\, A(r,\theta,\theta_0) + \psi\, B(r,\theta)) + \sin^2 z(\eta^2\, C(r,\theta,\theta_0) + \eta\psi\, D(r,\theta,\theta_0) + \psi^2\, E(r,\theta)). \tag{B 20}$$

The functions $C(r,\theta,\theta_0)$, $D(r,\theta,\theta_0)$, and $E(r,\theta)$ are given by

$$C(r,\theta,\theta_0) = \begin{cases} -\dfrac{1}{J_0^2(\mu_1)}\dfrac{2}{r^2}\,(C_1(r,\theta,\theta_0) + C_2(r,\theta,\theta_0) + C_3(r,\theta,\theta_0)), & r \leqslant 1, \\ \dfrac{1}{r^4}\left(6\cos(4\theta - 2\theta_0) + \dfrac{1}{r^2}\,(4 - 6\cos(2\theta - 2\theta_0))\right), & r > 1, \end{cases} \tag{B 21}$$

where

$$C_1(r,\theta,\theta_0) = J_0^2(\mu_1 r)\,(-2 - 3\cos(4\theta - 2\theta_0) + 3\cos(2\theta - 2\theta_0)),$$

$$C_2(r,\theta,\theta_0) = \frac{1}{\mu_1 r} J_0(\mu_1 r) J_1(\mu_1 r)\big(8 - \mu_1^2 r^2 + 6\cos(4\theta - 2\theta_0) - \big(12 - \mu_1^2 r^2\big)\cos(2\theta - 2\theta_0) + 2\mu_1^2 r^2 \cos 2\theta \sin^2(\theta - \theta_0)\big),$$

$$C_3(r,\theta,\theta_0) = \frac{1}{\mu_1^2 r^2} J_1^2(\mu_1 r)\big(-8 + 2\mu_1^2 r^2 + 12\cos(2\theta - 2\theta_0) + \mu_1^2 r^2(-4\cos(2\theta - \theta_0)\cos\theta_0 + \sin 2\theta \sin(2\theta - 2\theta_0))\big);$$

$$D(r,\theta,\theta_0) = \begin{cases} \dfrac{1}{J_0^2(\mu_1)}\dfrac{4}{r}\,(D_1(r,\theta,\theta_0) + D_2(r,\theta,\theta_0) + D_3(r,\theta,\theta_0),) & r \leqslant 1, \\ -\dfrac{4}{r^3}\left(\dfrac{1}{r^2}\cos(\theta - \theta_0) - 3\cos(3\theta - \theta_0)\right), & r > 1, \end{cases} \tag{B 22}$$

where

$$D_1(r,\theta,\theta_0) = J_0^2(\mu_1 r)\,(-\cos(\theta - \theta_0) + 3\cos(3\theta - \theta_0)),$$

$$D_2(r,\theta,\theta_0) = \frac{2}{\mu_1 r} J_0(\mu_1 r) J_1(\mu_1 r)\,(2\cos(\theta - \theta_0) - 3\cos(3\theta - \theta_0)),$$

$$D_3(r,\theta,\theta_0) = J_1^2(\mu_1 r)\left(\frac{3}{2}\cos(3\theta - \theta_0) + \frac{1}{2}\cos(\theta + \theta_0) - \frac{4}{\mu_1^2 r^2}\cos(\theta - \theta_0)\right);$$

and

$$E(r,\theta) = \begin{cases} \dfrac{4}{J_0^2(\mu_1)}\, E_1(r,\theta)\cos 2\theta, & r \leqslant 1, \\ \dfrac{4}{r^2}\cos 2\theta, & r > 1, \end{cases} \tag{B 23}$$

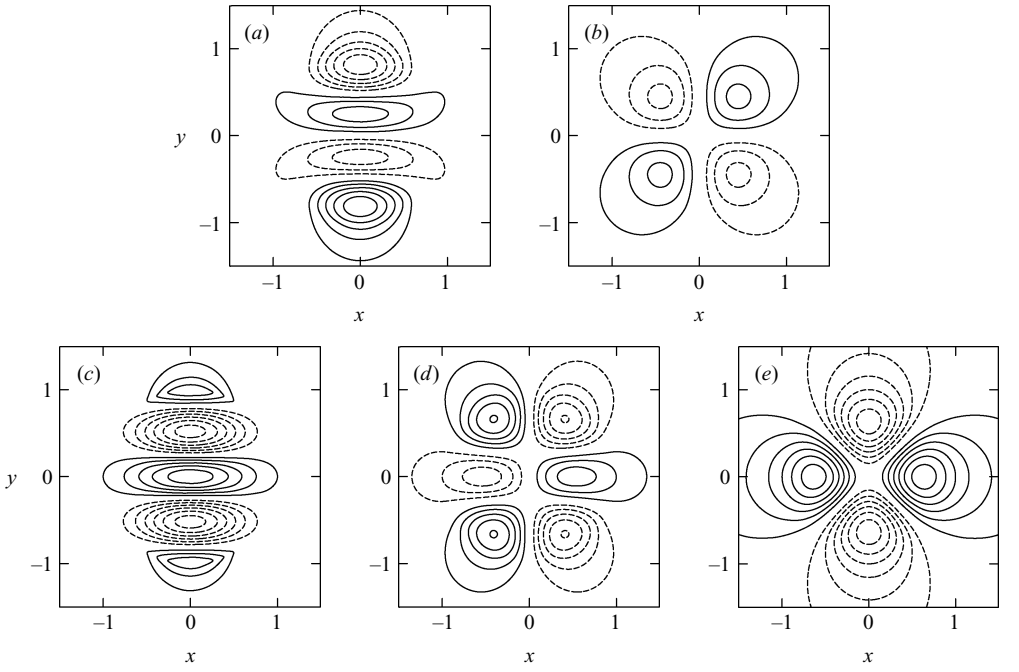


FIGURE 23. Functions $A(r,\theta,\theta_0=0)$ (*a*), $B(r,\theta)$ (*b*), $C(r,\theta,\theta_0=0)$ (*c*), $D(r,\theta,\theta_0=0)$ (*d*), and $E(r,\theta)$ (*e*). Contour spacings are 1 for (*a*), (*b*), (*e*), and 4 for (*c*), (*d*). Negative contours are dashed, and no zero contours are shown.

where

$$E_1(r,\theta)=\left(J_0^2(\mu_1 r)-\frac{2}{\mu_1 r}J_0(\mu_1 r)J_1(\mu_1 r)+J_1^2(\mu_1 r)\right).$$

The functions $A$ to $E$ are plotted in figure 23 for $\theta_0=0$, which is the case at the inflection levels whatever the value of $\psi$.

## REFERENCES


BASAK, S. & SARKAR, S. 2006 Dynamics of a stratified shear layer with horizontal shear. *J. Fluid Mech.* **568**, 19–54.

BATCHELOR, G. K. 1967 *An Introduction to Fluid Dynamics*. Cambridge University Press.

BAYLY, B. J. 1986 Three-dimensional instability of elliptical flows. *Phys. Rev. Lett.* **57**, 2160–2163.

BILLANT, P. BRANCHER, P. & CHOMAZ, J.-M. 1999 Three-dimensional stability of a vortex pair. *Phys. Fluids* **11**, 2069–2077.

BILLANT, P. & CHOMAZ, J.-M. 2000*a* Experimental evidence for a new instability of a vertical columnar vortex pair in a strongly stratified fluid. *J. Fluid Mech.* **418**, 167–188.

BILLANT, P. & CHOMAZ, J.-M. 2000*b* Theoretical analysis of the zigzag instability of a vertical columnar vortex pair in a strongly stratified fluid. *J. Fluid Mech.* **419**, 29–63.

BILLANT, P. & CHOMAZ, J.-M. 2000*c* Three-dimensional stability of a vertical columnar vortex pair in a stratified fluid. *J. Fluid Mech.* **419**, 65–91.

BILLANT, P. & CHOMAZ, J.-M. 2001 Self-similarity of strongly stratified inviscid flows. *Phys. Fluids* **13**, 1645–1651.

CHAPLYGIN, S. A. 1903 One case of vortex motion in a fluid. *Trans. Phys. Sect. Imperial Moscow Soc. Friends of Natural Sciences* **11** (2), 11–14.

Clyne, J. & Rast, M. 2005 A prototype discovery environment for analyzing and visualizing terascale turbulent fluid flow simulations. In *Visualization and Data Analysis 2005* (ed. R. F. Erbacher, J. C. Roberts, M. T. Gordon & K. Borner), pp. 284–294. SPIE.

Crow, S. C. 1970 Stability theory for a pair of trailing vortices. *AIAA J.* **8**, 2172–2179.

Deloncle, A., Billant, P. & Chomaz, J.-M. 2008 Nonlinear evolution of the zigzag instability in stratified fluids: A shortcut on the route to dissipation. *J. Fluid Mech.* **599**, 229–239.

Domaradzki, J. A., Xiao, Z. & Smolarkiewicz, P. K. 2003 Effective eddy viscosities in implicit large eddy simulations of turbulent flows. *Phys. Fluids* **15**, 3890–3893.

Drazin, P. G. 1961 On the steady flow of a fluid of variable density past an obstacle. *Tellus* **13**, 239–251.

Grinstein, F. F., Margolin, L. G. & Rider, W. J. (Ed.) 2007 *Implicit Large Eddy Simulation: Computing Turbulent Fluid Dynamics*. Cambridge University Press.

Herring, J. R. & Métais, O. 1989 Numerical experiments in forced stably stratified turbulence. *J. Fluid Mech.* **202**, 97–115.

Kelvin, Lord 1880 Vibrations of a columnar vortex. *Phil. Mag.* **10** (5), 155–168.

Kerswell, R. R. 2002 Elliptical instability. *Annu. Rev. Fluid Mech.* **34**, 83–113.

Lamb, H. 1895 *Hydrodynamics*, 2nd edn. Cambridge University Press.

Laporte, F. & Corjon, A. 2000 Direct numerical simulations of the elliptic instability of a vortex pair. *Phys. Fluids* **12**, 1016–1031.

Le Dizès, S. & Laporte, F. 2002 Theoretical predictions for the elliptical instability in a two-vortex flow. *J. Fluid Mech.* **471**, 169–201.

Leweke, T. & Williamson, C. H. K. 1998 Cooperative elliptic instability of a vortex pair. *J. Fluid Mech.* **360**, 85–119.

Lilly, D. K. 1983 Stratified turbulence and the mesoscale variability of the atmosphere. *J. Atmos. Sci.* **40**, 749–761.

Lindborg, E. 2006 The energy cascade in a strongly stratified fluid. *J. Fluid Mech.* **550**, 207–242.

Margolin, L. G., Rider, W. J. & Grinstein, F. F. 2006*a* Modeling turbulent flows with implicit LES. *J. Turbul.* **7** (15), 1–27.

Margolin, L. G., Smolarkiewicz, P. K. & Wyszogradzki, A. A. 2006*b* Dissipation in implicit turbulence models: A computational study. *Trans. ASME: J. Appl. Mech.* **73**, 469–473.

Margolin, L. G., Smolarkiewicz, P. K. & Wyszogrodzki, A. A. 2002 Implicit turbulence modeling for high Reynolds number flows. *Trans. ASME: J. Fluids Engng* **124**, 862–867.

Meleshko, V. V. & van Heijst, G. L. V. 1994 On Chaplygin's investigations of two-dimensional vortex structures in an inviscid fluid. *J. Fluid Mech.* **272**, 157–182.

Miyazaki, T. & Fukumoto, Y. 1992 Three-dimensional instability of strained vortices in a stably stratified fluid. *Phys. Fluids* A **4**, 2515–2522.

Moin, P. & Mahesh, K. 1998 Direct numerical simulation: A tool in turbulence research. *Annu. Rev. Fluid Mech.* **30**, 539–578.

Moore, D. W. & Saffman, P. G. 1975 The instability of a straight vortex filament in a strain field. *Proc. R. Soc. Lond.* A **346**, 413–425.

Ngan, K., Straub, D. N. & Bartello, P. 2005 Aspect ratio effects in quasi-two-dimensional turbulence. *Phys. Fluids* **17**, 125102.

Otheguy, P., Billant, P. & Chomaz, J.-M. 2006*a* The effect of planetary rotation on the zigzag instability of co-rotating vortices in a stratified fluid. *J. Fluid Mech.* **553**, 273–281.

Otheguy, P., Chomaz, J.-M. & Billant, P. 2006*b* Elliptic and zigzag instabilities on co-rotating vertical vortices in a stratified fluid. *J. Fluid Mech.* **553**, 253–272.

Pierrehumbert, R. T. 1986 Universal short-wave instability of two-dimensional eddies in an inviscid fluid. *Phys. Rev. Lett.* **57**, 2157–2159.

Prusa, J. M. & Smolarkiewicz, P. K. 2003 An all-scale anelastic model for geophysical flows: Dynamic grid deformation. *J. Comput. Phys.* **190**, 601–622.

Riley, J. J. & deBruynKops, S. M. 2003 Dynamics of turbulence strongly influenced by buoyancy. *Phys. Fluids* **15**, 2047–2059.

Riley, J. J., Metcalfe, R. W. & Weissman, M. A. 1981 Direct numerical simulations of homogeneous turbulence in density-stratified fluids. In *Nonlinear Properties of Internal Waves* (ed. B. J. West), pp. 79–112. APS.

Robinson, A. C. & Saffman, P. G. 1984 Three-dimensional stability of an elliptical vortex in a straining field. *J. Fluid Mech.* **142**, 451–466.

Schumann, U. 1991 Subgrid length-scales for large-eddy simulation of stratified turbulence. *Theor. Comput. Fluid Dyn.* **2**, 279–290.

Sipp, D. & Jacquin, L. 2003 Widnall instabilities in vortex pairs. *Phys. Fluids* **15**, 1861–1874.

Smolarkiewicz, P. K. 2006 Multidimensional positive definite advection transport algorithm: An overview. *Intl J. Numer. Meth. Fluids* **50**, 1123–1144.

Smolarkiewicz, P. K. & Grabowski, W. W. 1990 The multidimensional positive definite advection transport algorithm: Nonoscillatory option. *J. Comput. Phys.* **86**, 355–375.

Smolarkiewicz, P. K. & Margolin, L. G. 1993 On forward-in-time differencing for fluids: Extension to a curvilinear framework. *Mon. Wea. Rev.* **121**, 1847–1859.

Smolarkiewicz, P. K. & Margolin, L. G. 1998 MPDATA: A positive definite solver for geophysical flows. *J. Comput. Phys.* **140**, 459–480.

Smolarkiewicz, P. K. & Margolin, L. G. 2000 Variational methods for elliptic problems in fluid models. In *Proc. ECMWF Workshop on Developments in Numerical Methods for Very High Resolution Global Models*, pp. 137–159. Reading, UK: ECMWF.

Smolarkiewicz, P. K. & Margolin, L. G. 2007 Studies in geophysics. In *Implicit Large Eddy Simulation: Computing Turbulent Fluid Dynamics* (ed. F. F. Grinstein, L. Margolin & W. Rider). Cambridge University Press.

Smolarkiewicz, P. K., Margolin, L. G. & Wyszogrodzki, A. A. 2001 A class of nonhydrostatic global models. *J. Atmos. Sci.* **58**, 349–364.

Smolarkiewicz, P. K. & Prusa, J. M. 2002 Forward-in-time differencing for fluids: Simulations of geophysical turbulence. In *Turbulent Flow Computation* (ed. D. Drikakis & B. J. Guertz), pp. 279–312. Kluwer.

Smolarkiewicz, P. K. & Prusa, J. M. 2005 Towards mesh adaptivity for geophysical turbulence: Continuous mapping approach. *Intl J. Numer. Meth. Fluids* **47**, 789–801.

Smolarkiewicz, P. K., Sharman, R., Weil, J., Perry, S. G., Heist, D. & Bowker, G. 2007 Building resolving large-eddy simulations and comparison with wind tunnel experiments. *J. Comput. Phys.* **227**, 633–653.

Thomas, P. J. & Auerbach, D. 1994 The observation of the simultaneous development of a long- and a short-wave instability mode on a vortex pair. *J. Fluid Mech.* **265**, 289–302.

Tsai, C.-Y. & Widnall, S. E. 1976 The stability of short waves on a straight vortex filament in a weak externally imposed strain field. *J. Fluid Mech.* **73**, 721–733.

Vladimirov, V. A. & Il'in, K. I. 1988 Three-dimensional instability of an elliptic Kirchhoff vortex. *Fluid Dyns.* **23**, 356–360.

Waite, M. L. & Bartello, P. 2004 Stratified turbulence dominated by vortical motion. *J. Fluid Mech.* **517**, 281–308.

Waleffe, F. 1990 On the three-dimensional instability of strained vortices. *Phys. Fluids* A **2**, 76–80.

Warn-Varnas, A., Hawkins, J., Smolarkiewicz, P. K., Chin-Bing, S. A., King, D. & Hallock, Z. 2007 Solitary wave effects north of Strait of Messina. *Ocean Modell.* **18**, 97–121.

Wedi, N. P. & Smolarkiewicz, P. K. 2006 Direct numerical simulation of the Plumb-McEwan laboratory analog of the QBO. *J. Atmos. Sci.* **63**, 3226–3252.